


Phonon properties and thermal conductivity from first principles, lattice dynamics, and the Boltzmann transport equation

Cite as: J. Appl. Phys. **125**, 011101 (2019); <https://doi.org/10.1063/1.5064602>

Submitted: 05 October 2018 . Accepted: 11 December 2018 . Published Online: 03 January 2019

Alan J. H. McGaughey , Ankit Jain , Hyun-Young Kim, and Bo Fu (傅博)

COLLECTIONS

 This paper was selected as Featured



View Online



Export Citation



CrossMark

ARTICLES YOU MAY BE INTERESTED IN

[Nanoscale thermal transport. II. 2003–2012](#)

Applied Physics Reviews **1**, 011305 (2014); <https://doi.org/10.1063/1.4832615>

[Tutorial: Novel properties of defects in semiconductors revealed by their vibrational spectra](#)

Journal of Applied Physics **123**, 161561 (2018); <https://doi.org/10.1063/1.5011036>

[A practical field guide to thermoelectrics: Fundamentals, synthesis, and characterization](#)

Applied Physics Reviews **5**, 021303 (2018); <https://doi.org/10.1063/1.5021094>

Applied Physics Reviews
Now accepting original research

2017 Journal
Impact Factor:
12.894

Phonon properties and thermal conductivity from first principles, lattice dynamics, and the Boltzmann transport equation

Cite as: J. Appl. Phys. **125**, 011101 (2019); doi: [10.1063/1.5064602](https://doi.org/10.1063/1.5064602)

Submitted: 5 October 2018 · Accepted: 11 December 2018 ·

Published Online: 3 January 2019



Alan J. H. McGaughey,^{1,a)}  Ankit Jain,¹  Hyun-Young Kim,¹ and Bo Fu (傅博)^{1,2}

AFFILIATIONS

¹Department of Mechanical Engineering, Carnegie Mellon University, Pittsburgh, Pennsylvania 15213, USA

²MOE Key Laboratory of Thermo-Fluid Science and Engineering, School of Energy and Power Engineering, Xi'an Jiaotong University, Xi'an 710049, China

^{a)}Electronic mail: mcgaughey@cmu.edu.

ABSTRACT

A computational framework for predicting phonon frequencies, group velocities, scattering rates, and the resulting lattice thermal conductivity is described. The underlying theory and implementation suggestions are also provided. By using input from first principles calculations and taking advantage of advances in computational power, this framework has enabled thermal conductivity predictions that agree with experimental measurements for diverse crystalline materials over a wide range of temperatures. Density functional theory and density functional perturbation theory calculations are first used to obtain the harmonic and cubic force constants. The harmonic force constants are the input to harmonic lattice dynamics calculations, which provide the phonon frequencies and eigenvectors. The harmonic properties and the cubic force constants are then used with perturbation theory and/or phenomenological models to determine intrinsic and extrinsic scattering rates. The full set of phonon properties is then used to solve the Boltzmann transport equation for the mode populations and thermal conductivity. The extension of the framework to include higher-order processes, capture finite temperature effects, and model alloys is described. A case study on silicon is presented that provides benchmarking and convergence data. Available packages that implement the framework are compared.

Published under license by AIP Publishing. <https://doi.org/10.1063/1.5064602>

I. INTRODUCTION

The objective of this tutorial is to describe a computational framework based on first principles calculations, lattice dynamics calculations, and the Boltzmann transport equation (BTE) for predicting the thermal conductivity \mathbf{k} of a crystalline solid where phonons, the quanta of energy associated with atomic vibrations, are the dominant energy carriers.

Thermal conductivity is defined as the ratio of the heat flux \mathbf{Q} in a material to the temperature gradient ∇T by the Fourier law

$$\mathbf{Q} = -\mathbf{k}\nabla T. \quad (1)$$

Thermal conductivity is a second-order tensor with zero

non-diagonal elements $k_{\alpha\beta} \equiv k_{\beta\alpha}$, where $\alpha = x, y,$ or z . Thermal conductivity is a function of thermodynamic state (i.e., temperature and pressure) and reflects processes happening at the scale of the fundamental energy carriers. In a crystalline solid, the carriers are electrons and phonons, the latter of which is the focus here. Thermal transport by phonons is relevant in a wide range of applications. Thermal insulation and thermoelectric energy conversion require low thermal conductivity. Heat dissipation in the semiconductor layers in microelectronic and optoelectronic energy conversion devices requires high thermal conductivity. Experimentally-measured thermal conductivities of crystals where phonons dominate thermal transport are plotted in [Fig. 1](#).¹⁻¹⁰

Phonon dynamics are governed by the BTE. The thermal conductivity prediction framework discussed herein is

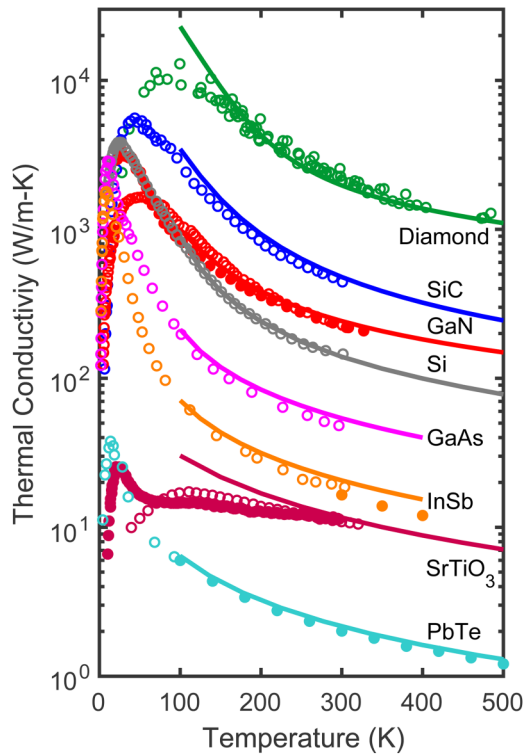


FIG. 1. Thermal conductivity data from experimental measurements (markers) and first principles-driven predictions (lines) for diamond,¹¹ SiC,^{5,12} GaN,^{6,7,12} Si,⁸ GaAs,^{2,12} InSb,^{2,3,12} SrTiO₃,^{9,10,13} and PbTe.^{1,4,14} The diamond experimental data are from five sources, which are distinguished in Ref. 11. Two sets of experimental data are shown and distinguished for each of GaN, InSb, SrTiO₃, and PbTe. The silicon predictions were made using the framework described herein. All experimental data are for materials that contain their natural isotopic content. The predictions for diamond, SiC, GaN, Si, GaAs, and InSb include the effect of isotope scattering.

based on a steady-state analysis, where the BTE for a phonon mode with wave vector \mathbf{q} and polarization denoted by ν is¹⁵

$$\mathbf{v}_g(\mathbf{q}_\nu) \cdot \nabla n(\mathbf{q}_\nu) = \left[\frac{\partial n(\mathbf{q}_\nu)}{\partial t} \right]_{\text{collision}}. \quad (2)$$

The left-hand side represents phonon drift, where \mathbf{v}_g is the mode's group velocity vector and n is its population. The right-hand side captures phonon scattering and is called the collision term. The collision term represents a complicated set of phenomena and is not a derivative per se. Equation (2) is written for all phonon modes in the crystal, and the set of coupled differential equations are solved for the unknown populations.

The phonon heat flux is found by summing over all modes as

$$\mathbf{Q} = \frac{1}{V} \sum_{\mathbf{q}, \nu} \hbar \omega(\mathbf{q}_\nu) \mathbf{v}_g(\mathbf{q}_\nu) n(\mathbf{q}_\nu), \quad (3)$$

where V is the crystal volume, \hbar is the reduced Planck constant, and ω is the mode frequency. At equilibrium, i.e., when the temperature gradient is zero, $\mathbf{Q} = \mathbf{0}$ and the populations are described by the Bose-Einstein distribution

$$n_{\text{BE}}(\mathbf{q}_\nu) = \frac{1}{e^x - 1}, \quad (4)$$

where $x = \hbar \omega(\mathbf{q}_\nu) / k_B T$, k_B is the Boltzmann constant, and T is the temperature.

By solving a linearized form of Eq. (2) and using Eqs. (1) and (3), the thermal conductivity in direction α can be written as

$$k_\alpha = \sum_{\mathbf{q}, \nu} c(\mathbf{q}_\nu) v_{g,\alpha}^2(\mathbf{q}_\nu) \tau_\alpha(\mathbf{q}_\nu). \quad (5)$$

Here, c is the volumetric specific heat, which is a function of temperature and frequency, and τ_α is the lifetime (which is also called the scattering time or the transport lifetime) when the heat flux is applied in the α -direction.

The theoretical pieces needed to predict the phonon properties in Eq. (5) and the resulting thermal conductivity have existed for many decades but were not integrated until the late 2000s. The underlying theory is described in previous papers and reviews,^{12,15-19} such that we only present an overview. Our focus is on the computational workflow, which is shown in Fig. 2 and contains two parts: first, calculating the atomic force constants from an empirical potential or first principles and second, using the force constants to calculate phonon properties and from these, thermal conductivity. It is important to note that the lattice dynamics calculations and BTE solutions associated with the second part of the workflow are agnostic to the origin of the force constants. The scalings of the computational cost of the central elements of the framework are presented in Table I.

The historical use of empirical potentials (e.g., Stillinger-Weber or Tersoff for silicon) and/or the relaxation time approximation (RTA) led to thermal conductivity predictions that deviated significantly from measurements.²²⁻²⁴ These deviations are largely a result of empirical potentials not being fit to thermal transport-related properties. It was not until (i) force constants obtained from first-principles calculations [e.g., based on density functional theory (DFT) and density functional perturbation theory (DFPT)]^{16,25} and (ii) solutions of the BTE beyond the RTA,²⁶⁻²⁸ both of which were enabled by advances in computational power, were applied that thermal conductivity predictions began to agree with measurements. The success of the first-principles driven framework has since been demonstrated for a range of low and high thermal conductivity materials, examples of which are provided in Fig. 1 alongside the experimental measurements.¹¹⁻¹⁴ We will return to a discussion of Fig. 1 in Sec. V E.

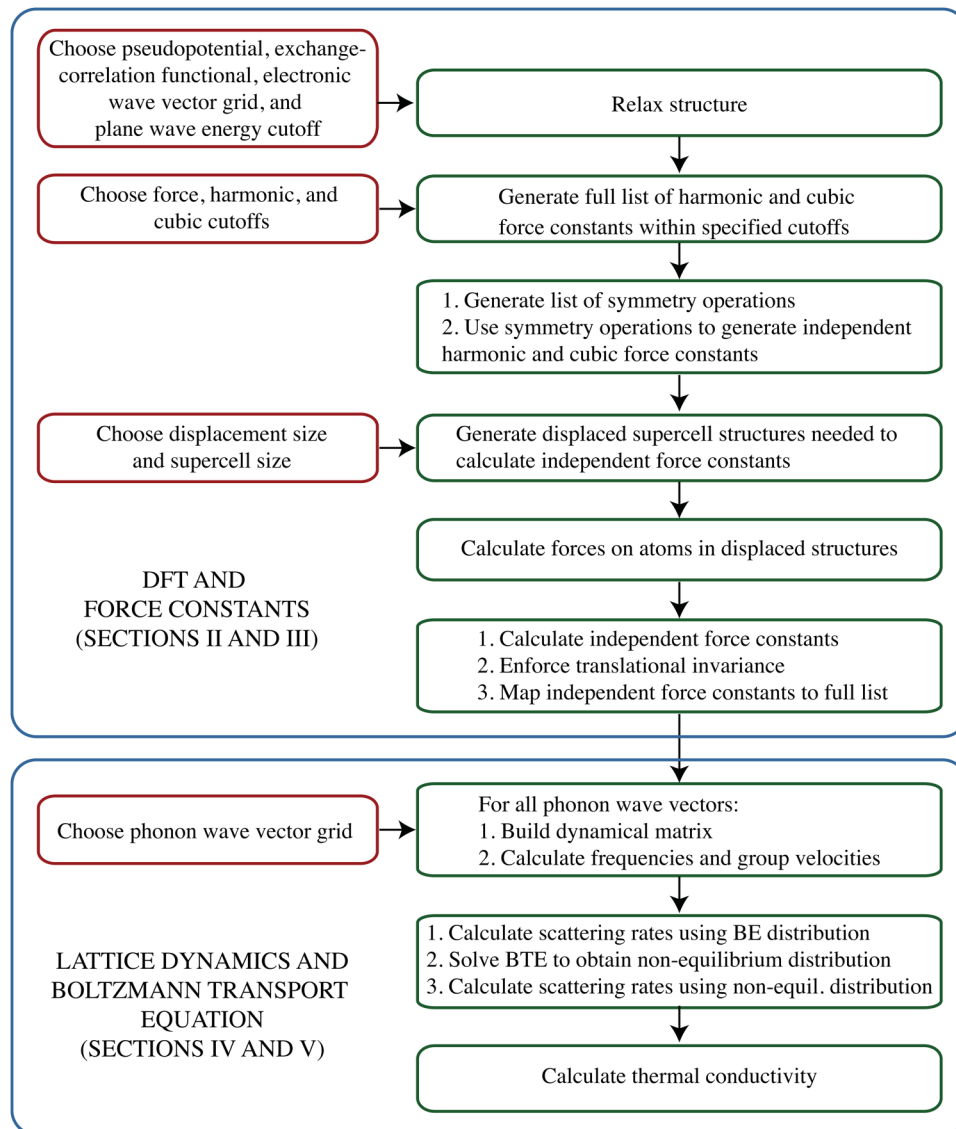


FIG. 2. Workflow for obtaining phonon properties and thermal conductivity from density functional theory (DFT) calculations, lattice dynamics calculations, and the BTE. The harmonic force constants can alternatively be calculated from density functional perturbation theory (DFPT), which may provide better accuracy. A similar workflow can be used with empirical potentials, with the only difference being how the forces are calculated.

While open-source packages are now available that allow for thermal conductivity predictions to be made with reasonable ease (e.g., ALAMODE,²⁹ almaBTE,³⁰ phono3py,³¹ and ShengBTE³²), the user must still make key decisions throughout the workflow. It is our hope that this tutorial will help users of these packages to understand (i) how to make these decisions, (ii) how to ensure convergence, and (iii) the trade-offs between accuracy and computational cost. This tutorial should also be helpful to researchers who are developing their own computational tools and integrating them with available packages.

The rest of the tutorial is organized as follows. The set-up of the DFT calculations is discussed in Sec. II. The force constant calculation is motivated in the context of a Taylor series expansion of potential energy and described in Sec. III. The harmonic lattice dynamics calculations that provide the phonon frequencies are described in Sec. IV. Calculations of phonon scattering rates due to intrinsic and extrinsic factors are presented in the context of the linearized BTE, perturbation theory, and phenomenological models in Sec. V, which lead to the final thermal conductivity

TABLE I. Computational cost scaling of the central elements of the thermal conductivity prediction framework. N_{total} is the total number of atoms in the computational cell, $N_{unitcell}$ is the number of atoms in the unit cell, and M is the number of wave vectors. For a Brillouin zone resolution of $q_x \times q_y \times q_z$, $M = q_x q_y q_z$.

Calculation	Scaling	Comment
DFT (single point energy)	N_{total}^3	DFT codes that scale as N_{total} are available, ²⁰ although large N_{total} is required to realize the benefits.
DFPT	N_{total}^4	Typically, $N_{total} = N_{unitcell}$. An N_{total}^3 scaling algorithm has been proposed. ²¹
Harmonic lattice dynamics	$N_{unitcell}^3 M$	Required in RTA and full BTE solutions.
Three-phonon scattering rates	$N_{unitcell}^4 M^2$	

prediction. Advanced topics are discussed in Sec. VI. A case study for silicon is presented in Sec. VII, which provides benchmarking data and an examination of convergence. A survey of computational packages is presented in Sec. VIII and a summary and outlook are provided in Sec. IX.

II. DENSITY FUNCTIONAL THEORY

Predicting phonon properties and thermal conductivity requires a calculator that provides the energy of a set of atoms and, ideally, the net force exerted on each atom. Density functional theory is a suitable calculator for this purpose.^{33,34} Within the framework of DFT, the many-body problem of interacting electrons described by the Schrödinger equation is reduced to a simpler problem of non-interacting electrons in an effective potential. It is because DFT includes electronic degrees of freedom that it is more accurate than empirical potentials, but also what makes it more computationally expensive.

As related to phonon properties and thermal conductivity, DFT is applied to perform: (i) An energy minimization to obtain the zero-temperature atomic structure. It is common practice to use the zero-temperature structure for predicting phonon properties and thermal conductivity at finite temperatures. Finite temperature effects are discussed in Sec. VI B. (ii) Single point energy/force calculations that provide the force constants

through finite differences (Sec. III C). The force constants can also be obtained from DFPT calculations (Sec. III B).^{35,36}

The DFT package must first be selected. Common packages are listed in Table II along with key features and capabilities. While we present DFT calculations performed using the plane wave package Quantum ESPRESSO,³⁷ the computational framework can be applied using any DFT package that can handle periodic systems. When benchmarking results, it is important to ensure that the same version of a package is used.

In a plane wave-based DFT code, the pseudopotential and exchange-correlation functional must be selected. A pseudopotential is specified for each atomic species and approximates the Coulombic potential for the nucleus and the core electrons by considering them together. This choice reduces the computational cost compared to all-electron methods by enabling the use of plane-wave basis sets for describing the valence electrons. The exchange-correlation functional approximates the many-body electron interactions. Its specification remains the major challenge in DFT. The simplest form of the exchange-correlation is the local density approximation (LDA),⁴⁷ in which the effective potential is only a function of the spatially-dependent electron density. The generalized gradient approximation (GGA), of which there are many varieties,^{48,49} uses the electron density and its gradient. Additional complexity can be added beyond the GGA, as described by the Jacob's ladder of density functional approximations.⁵⁰ Density functional theory packages typically contain a library of pseudopotentials and multiple options for the exchange-correlation functional.

Selecting the pseudopotential and exchange-correlation functional in a DFT calculation is analogous to selecting an empirical potential. Reported accuracies of a given pseudopotential and exchange-correlation functional for material properties not directly related to thermal transport (e.g., elastic constants, defect energies) may not be a good gauge of their suitability for predicting phonon properties and thermal conductivity due to the key role played by anharmonicity. Recent studies have assessed the impact of the pseudopotential and exchange-correlation functional on thermal conductivity prediction. For silicon at a temperature of 300 K, Jain and McGaughey report a range of 127–172 W/m K.⁵¹ For graphene at a temperature of 300 K, Qin *et al.* report a range of

TABLE II. Density functional theory packages and their features/capabilities.

	Quantum ESPRESSO ³⁷	GPAW ^{38,39}	VASP ^{40–43,c}	FHI-aims ⁴⁴	ABINIT ⁴⁵
Basis set	Plane wave	Plane wave, LCAO, ^a real-space mesh	Plane wave	All-electron	Plane wave
Open source	Yes	Yes	No	No	Yes
GPU ^d compatibility	Yes (3rd party)	Partial	Partial	Partial	Experimental
Vibrational frequencies	DFPT, 3rd-order for cubic force constants also available	Finite difference when combined with ASE ^b	Finite difference, DFPT (Γ -point only)	Finite difference, DFPT (Γ -point only)	DFPT

^aLinear combination of atomic orbitals.

^bAtomic simulation environment.⁴⁶

^cVienna Ab Initio Simulation Package.

^dGraphics processing unit.

1900–4440 W/mK,⁵² while Taheri *et al.* report a range of 5400–8700 W/mK.⁵³

Two key parameters must be specified in any plane wave-based DFT calculation: (i) The electronic wave vector grid, which provides the resolution of the electronic Brillouin zone. Its specification depends on the material and the size of the computational cell. Smaller computational cells require a finer electronic wave vector grid. (ii) The plane wave energy cutoff, which truncates the expansion of the wave functions of the valence electrons. Its specification depends on the material and the choice of pseudopotential. Softer pseudopotentials require a smaller plane wave energy cutoff.⁵⁴ When modeling a low-dimensional material (e.g., a carbon nanotube or graphene), the size of the surrounding vacuum region must also be specified. The electronic wave vector grid, the plane wave energy cutoff, and the vacuum size should be chosen to ensure convergence of properties of interest.

III. FORCE CONSTANTS

A. Taylor series expansion of potential energy

The material-dependent inputs to the workflow shown in Fig. 2 are its crystal structure and force constants. The unit cell parameters and equilibrium atomic positions can be obtained from an energy minimization in DFT. To understand the need for the force constants, consider a Taylor series expansion of the potential energy of the system, U , around its equilibrium state

$$U = U_0 + \sum_i \sum_\alpha \Pi_i^\alpha u_i^\alpha + \frac{1}{2!} \sum_{ij} \sum_{\alpha\beta} \Phi_{ij}^{\alpha\beta} u_i^\alpha u_j^\beta + \frac{1}{3!} \sum_{ijk} \sum_{\alpha\beta\gamma} \Psi_{ijk}^{\alpha\beta\gamma} u_i^\alpha u_j^\beta u_k^\gamma + \dots, \quad (6)$$

where

$$\Pi_i^\alpha = \frac{\partial U}{\partial u_i^\alpha} = -F_i^\alpha, \quad (7)$$

$$\Phi_{ij}^{\alpha\beta} = \frac{\partial^2 U}{\partial u_i^\alpha \partial u_j^\beta}, \quad (8)$$

$$\Psi_{ijk}^{\alpha\beta\gamma} = \frac{\partial^3 U}{\partial u_i^\alpha \partial u_j^\beta \partial u_k^\gamma}. \quad (9)$$

Here, i , j , and k sum over the atoms and α , β , and γ sum over the Cartesian coordinates (x , y , and z). U_0 is the reference energy, which is taken as zero, and u_i^α labels a small displacement of atom i in the α -direction. Π_i^α is the negative of the net force acting on atom i in the α -direction, F_i^α , which is zero at equilibrium. The $\Phi_{ij}^{\alpha\beta}$ and $\Psi_{ijk}^{\alpha\beta\gamma}$ terms are the second- and third-order derivatives of the potential energy and are known as the harmonic and cubic force constants.

Each summation in Eq. (6) is in theory infinite. In practice, phonon property and thermal conductivity calculations (Secs. IV and V) are made by considering interactions between atoms within a cutoff radius in a supercell (i.e., a computational cell built from many unit cells), leading to a finite number of force constants. Even then, the number of atoms required to obtain converged phonon properties and thermal conductivity may be $O(100)$, such that the number of unknown force constants is intractable. To make computations feasible, it is imperative to use permutation (e.g., $\Phi_{ij}^{\alpha\beta} = \Phi_{ji}^{\beta\alpha}$) and space group symmetries (using, e.g., Spglib⁵⁵) to reduce the number of unknown force constants.⁵⁶ The number of distinct force constant depends on the size and symmetry of the unit cell. Silicon has a two-atom face-centered cubic unit cell. By considering fifth- (6.21 Å) and third- (4.86 Å) neighbor cutoffs for the harmonic and cubic force constants, symmetries reduce the number of unknown force constants from 3384 and 90 936 to 17 and 95. β -Ga₂O₃ has a ten-atom monoclinic unit cell with comparatively less symmetry than silicon. By considering 11 Å and 3 Å cutoffs for the harmonic and cubic force constants, symmetries reduce the number of unknown force constants from 46 566 and 11 448 to 11 836 and 1198.

The harmonic and cubic force constants also need to satisfy translational invariance, which dictates that translating the crystal as a whole leaves the force constants unchanged. Not satisfying translational invariance can lead to unphysical results such as non-zero acoustic frequencies at the Γ -point (i.e., the center of the Brillouin zone). When extracting force constants numerically, translational invariance is not satisfied due to finite numerical precision. Translational invariance can be satisfied by either (i) using it along with the symmetry constraints to reduce the number of unknown force constants⁵⁶ or (ii) as a post-extraction step in which small corrections are added to all force constants.⁵⁷

We next describe how the harmonic and cubic force constants can be obtained at zero temperature using DFPT, which is a DFT-based reciprocal space approach, and using finite displacements, which is a real space approach that can be applied using both DFT and empirical potentials. The quasi-harmonic approximation and finite-temperature force constant calculations are described in Sec. VI B.

B. Density functional perturbation theory

In DFPT, linear response theory is applied to the Kohn-Sham equations used to solve for the electronic charge density to determine how the solutions are affected by small perturbations.^{35,36} It can be applied to study phonons, electric field response, and phonon-electron coupling. Specific to this tutorial, the force constants are related to the derivatives of the electronic charge density with respect to atomic displacements. The calculation is made in reciprocal space at the level of the unit cell, which allows for calculation of dynamical matrices at an arbitrary resolution of the phonon Brillouin zone without the need for supercells. An inverse Fourier transform is then applied to obtain the real space force constants. DFPT calculations scale with the fourth power of the number of atoms

in the unit cell, such that they are limited to small unit cell crystals. Calculation of harmonic force constants from DFPT is available in many DFT packages (Table II). The theory for obtaining cubic force constants from DFPT has been developed and its implementation into DFT packages is ongoing.

C. Finite displacements

1. Formulation

For an empirical potential, it is possible to determine the harmonic and cubic force constants analytically. The required derivatives, however, may be challenging to derive. As such, a more intuitive way to calculate the force constants, from either an empirical potential or DFT, is by applying small displacements to the atoms in a supercell. In doing so, it is convenient to note that

$$F_i^\alpha = -\frac{\partial U}{\partial u_i^\alpha} \approx -\sum_j \sum_\beta \Phi_{ij}^{\alpha\beta} u_j^\beta - \frac{1}{2} \sum_{j,k} \sum_{\beta,\gamma} \Psi_{ijk}^{\alpha\beta\gamma} u_j^\beta u_k^\gamma \quad (10)$$

and that

$$\Phi_{ij}^{\alpha\beta} = \frac{\partial^2 U}{\partial u_i^\alpha \partial u_j^\beta} = -\frac{\partial F_i^\alpha}{\partial u_j^\beta}, \quad (11)$$

$$\Psi_{ijk}^{\alpha\beta\gamma} \approx \frac{1}{4h^2} \left[F_i^\alpha(u_j^\beta = h, u_k^\gamma = -h) - F_i^\alpha(u_j^\beta = h, u_k^\gamma = h) + F_i^\alpha(u_j^\beta = -h, u_k^\gamma = h) - F_i^\alpha(u_j^\beta = -h, u_k^\gamma = -h) \right]. \quad (14)$$

3. Taylor series fitting

In the Taylor series fitting method, the harmonic and cubic force constants are obtained simultaneously by creating a set of supercells that have one or more atoms displaced from their equilibrium positions.⁵⁶ Equation (10) is then written as the linear system

$$\mathbf{U}\Phi = -\mathbf{F}, \quad (15)$$

where \mathbf{U} is the displacement matrix and contains terms of the form u_j^β and $u_j^\beta u_k^\gamma$, Φ is a vector that contains the unknown force constants, and \mathbf{F} is the force matrix, which contains terms of the form F_i^α . The number of rows in the displacement and force matrices is the number of force-displacement equations. For a three-dimensional system with N_{total} atoms in the supercell and N_s displaced supercells, the number of force-displacement equations is $3N_{total}N_s$. The number of columns in the displacement and force matrices is the number of unknown force constants (harmonic and cubic). If the number of unknown force constants is less than the number of equations, this linear system is over-specified and can be solved using least-square fitting (e.g., singular value decomposition).

$$\Psi_{ijk}^{\alpha\beta\gamma} = \frac{\partial^3 U}{\partial u_i^\alpha \partial u_j^\beta \partial u_k^\gamma} = -\frac{\partial^2 F_i^\alpha}{\partial u_j^\beta \partial u_k^\gamma}. \quad (12)$$

Thus, the harmonic and cubic force constants are related to the first and second derivatives of the forces. In a self-consistent DFT calculation, the forces can be obtained from the Hellman-Feynman theorem.

2. Finite difference

In the finite difference method, the harmonic (cubic) force constants are individually and directly evaluated by applying small displacements, h , to one (two) atoms in a supercell, calculating the resulting force on a second (third) atom, and then using a finite difference formula. We have found that four-point central difference formulas with a suitable choice of h provide sufficient accuracy. They are given by

$$\Phi_{ij}^{\alpha\beta} \approx \frac{F_i^\alpha(u_j^\beta = 2h) - 8F_i^\alpha(u_j^\beta = h) + 8F_i^\alpha(u_j^\beta = -h) - F_i^\alpha(u_j^\beta = -2h)}{12h}, \quad (13)$$

4. Implementation

To obtain the force constants from the finite difference or Taylor series fitting methods, the displacement size and the supercell size must be specified.

The displacement should be (i) large enough to avoid numerical uncertainties associated with the force calculations, which is more likely to be important in DFT than with an empirical potential and (ii) small enough that the atoms do not explore parts of the potential energy surface that have contributions beyond the cubic terms in Eq. (6). The magnitude of the appropriate displacement is material dependent. A suitable starting point is 0.01-0.05 Å.

Interactions between atoms grow weaker as the distance between them increases. When using an empirical potential, a radial cutoff is specified to limit the range of the interactions. The cutoff should be at most one half of the shortest linear dimension of the supercell to avoid an atom interacting with images of itself due to the required use of periodic boundary conditions. If long-range interactions are included using a reciprocal-space approach (e.g., electrostatic interactions modeled using the Ewald sum), then additional theory is required.³⁵

In a DFT calculation, an atom naturally interacts with all other atoms, including images of itself and other atoms in the image cells. There is no way to limit the extent of the interactions, as can be done for an empirical potential. The net force on an atom obtained from the Hellman-Feynman theorem includes the effect of all atoms in the supercell and in all the image cells.

Three cutoffs are required to enable tractable calculations of phonon properties and thermal conductivity from DFT-based force constants, which in turn inform the selection of the supercell size.

The *force cutoff* specifies the pairs and triplet of atoms to consider when forming the list of unknown force constants. The objective is to minimize the effect of images of the displaced atom(s). By Newton's third law, the sum of the forces acting on all the atoms in the supercell must be zero. Furthermore, the effect of displacing one atom on the force on another decreases as the distance between them increases. As such, the force cutoff should be chosen such that the sum of the forces on the atoms inside of its spherical volume is close to zero. To avoid an atom interacting with itself, the force cutoff should be at most one half of the smallest linear dimension of the supercell. Because of the potentially long-range interactions in a DFT system, the net force on an atom due to just the other atoms in the supercell is not necessarily zero. Thus, both the supercell size and the force cutoff must be simultaneously considered when assessing convergence of phonon properties and thermal conductivity.

The *harmonic cutoff* specifies the number of neighbor shells considered when performing harmonic lattice dynamics calculations (Sec. IV). The *cubic cutoff* specifies the number of neighbor shells considered when calculating phonon scattering rates using the BTE (Sec. V).

None of these three cutoffs limits the range of the atomic interactions in a DFT calculation. The maximum value of the harmonic or cubic cutoff is that of the force cutoff but can be less. For example: (i) When using the Taylor series fitting method (Sec. III C 3), a force cutoff that is larger than the harmonic and cubic cutoffs may provide higher accuracy force constants. (ii) The computational cost of the intrinsic scattering rate calculations (Sec. V A), which require cubic force constants, is large. Fortunately, cubic force constants tend to be short-range, which enables converged results for a cubic cutoff that is smaller than the force and harmonic cutoffs.

To get an idea about the range of the forces, consider the following example for silicon. We displaced one atom in a cubic 216-atom supercell (linear dimension of 16.2 Å) from its equilibrium position by 0.032 Å. The magnitude of the force acting on each of the 216 atoms in the supercell, including the displaced atom, is plotted versus the distance from the displaced atom in Fig. 3. The forces go to less than 1% of the maximum force (which is that acting on the displaced atom itself) beyond a distance of ~ 5 Å, which captures up to fourth neighbor interactions. This simple calculation, whose computational cost is insignificant compared to that for the

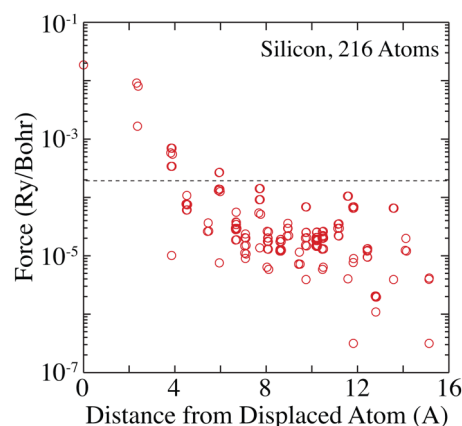


FIG. 3. Forces acting on the atoms in a 216-atom silicon supercell when one atom is displaced by 0.032 Å. The distance is calculated with respect to the displaced atom. The horizontal dashed line is to guide the eye and represents 1% of the maximum force.

full thermal conductivity prediction, provides a suggestion for the initial guesses for the force cutoff and supercell size for this system. As we will see in Sec. IV, however, while 5 Å is a suitable cubic cutoff for silicon, it is not sufficient for the harmonic cutoff.

IV. HARMONIC LATTICE DYNAMICS

A. Eigenvalue problem

The purpose of a harmonic lattice dynamics calculation is to determine the set of phonon frequencies ω and eigenvectors \mathbf{e} associated with the wave vector \mathbf{q} that define the modes (\mathbf{q}, ν) .⁵⁸ There are $3N_{\text{unitcell}}$ modes for a given wave vector. The eigenvector for each mode, which is also called the mode shape or polarization vector, is a vector of length $3N_{\text{unitcell}}$ whose entries are the relative displacements of the atoms when that mode is activated.

The choice of the unit cell sets the lattice vectors, the reciprocal lattice vectors, as thus the shape of the Brillouin zone and the allowed wave vectors.⁵⁹ For a desired Brillouin zone resolution, the full list of non-degenerate wave vectors needed to perform thermal transport calculations can be obtained by applying the Monkhorst-Pack algorithm.⁶⁰ A reduced list of wave vectors, which can significantly reduce the computational time required to calculate phonon scattering rates (Sec. V), can be obtained by applying the crystal symmetries.

A harmonic lattice dynamics calculation is performed at zero temperature, where the atoms sit at their equilibrium positions. By assuming that the phonon modes are non-interacting plane waves [i.e., independent harmonic oscillators, thus truncating the expansion in Eq. (6) after the second-order term], the solution of the resulting

eigenvalue problem,

$$\omega^2 \begin{pmatrix} \mathbf{q} \\ \nu \end{pmatrix} \mathbf{e} \begin{pmatrix} \mathbf{q} \\ \nu \end{pmatrix} = \mathbf{D}(\mathbf{q}) \mathbf{e} \begin{pmatrix} \mathbf{q} \\ \nu \end{pmatrix}, \quad (16)$$

gives the frequencies and eigenvectors for the wave vector \mathbf{q} . The dynamical matrix $\mathbf{D}(\mathbf{q})$ has size $3N_{\text{unitcell}} \times 3N_{\text{unitcell}}$ and is built from the harmonic force constants and the equilibrium atomic positions. The element of $\mathbf{D}(\mathbf{q})$ associated with the interaction of atoms b and b' ($1 \leq b, b' \leq N_{\text{unitcell}}$, b may be equal to b') where b is moving in the α -direction and b' is moving in the β -direction is given by

$$D_{3(b-1)+\alpha, 3(b'-1)+\beta}(bb', \mathbf{q}) = \frac{1}{(m_b m_{b'})^{1/2}} \sum_l \Phi_{b0, b'l}^{\alpha\beta} \exp\{i\mathbf{q} \cdot [\mathbf{r}(l) - \mathbf{r}(0)]\}. \quad (17)$$

Here, in the D subscript, α or β equals 1 for x , 2 for y , and 3 for z , m is the atomic mass, $\mathbf{r}(l)$ corresponds to the center of mass of unit cell l , the summation is over all unit cells, and the harmonic force constant corresponds to the α - β interaction between atom b in the central unit cell (denoted by 0) and atom b' in unit cell l . This formulation can also be used to predict the vibrational modes of a molecule by setting $\mathbf{q} = \mathbf{0}$ and taking the molecule as the unit cell.

Because the dynamical matrix is Hermitian, all its eigenvalues $\omega^2 \begin{pmatrix} \mathbf{q} \\ \nu \end{pmatrix}$ are real. For a crystal, three frequencies will always be zero, corresponding to the degrees of freedom associated with rigid translation. For a stable crystal, all the remaining eigenvalues are positive, leading to all positive frequencies. The presence of negative eigenvalues leads to imaginary frequencies. The associated modes are unstable and are an indication of a potential phase transition. Unstable modes do not have well-defined properties and prevent the calculation of thermal conductivity.

B. Property calculation

With the frequencies and eigenvectors for a full list of non-degenerate wave vectors in the Brillouin zone, harmonic-level phonon properties can be calculated. Because the lattice dynamics calculation does not make any assumptions about the system, Bose-Einstein (i.e., quantum) statistics can be used in these calculations. For comparing results to the predictions of classical molecular dynamics simulations, Boltzmann statistics should be used.

Plotting the phonon frequencies versus the wave vector along a given direction gives the phonon dispersion. The dispersion is typically plotted along high-symmetry directions, for example, a Γ -X-W-L- Γ loop for a face-centered cubic crystal.

The volumetric specific heat of a phonon mode is given by

$$c \begin{pmatrix} \mathbf{q} \\ \nu \end{pmatrix} = \hbar \omega \begin{pmatrix} \mathbf{q} \\ \nu \end{pmatrix} \frac{dn_{\text{BE}}}{dT} = \frac{k_B x^2}{V} \frac{e^x}{(e^x - 1)^2}. \quad (18)$$

In the classical limit, $c \begin{pmatrix} \mathbf{q} \\ \nu \end{pmatrix} = k_B T/V$. The volumetric specific

heat of the system can then be evaluated from

$$c = \sum_{\mathbf{q}, \nu} c \begin{pmatrix} \mathbf{q} \\ \nu \end{pmatrix}. \quad (19)$$

Similar formulas are available for calculating other thermodynamic quantities at the mode and system level (e.g., internal energy, Helmholtz free energy, entropy).⁶¹

The phonon group velocity is defined as

$$\mathbf{v}_g \begin{pmatrix} \mathbf{q} \\ \nu \end{pmatrix} = \frac{\partial \omega \begin{pmatrix} \mathbf{q} \\ \nu \end{pmatrix}}{\partial \mathbf{q}}, \quad (20)$$

which is the gradient of the dispersion curve. It can be calculated by two approaches.

The first approach is to perform a central difference on Eq. (20) using closely-space wave vectors. This technique is advantageous as no additional computational framework is needed beyond the solution of the eigenvalue problem. The disadvantage is that there is ambiguity when performing the central difference near where two dispersion branches cross. This ambiguity exists because eigenvalue solvers provide their output without any knowledge of the specific modes. This challenge can be overcome by using very small changes in the wave vector when performing the central difference and using the mode shapes to differentiate branches. For modes at the center or edge of the Brillouin zone, a forward or backward difference must be used. Care must also be taken near local minima or maxima, where the group velocity is zero.

The second approach is to evaluate the components of the group velocity vector using the expression⁶²

$$v_{g,\alpha} \begin{pmatrix} \mathbf{q} \\ \nu \end{pmatrix} = \frac{1}{2\omega \begin{pmatrix} \mathbf{q} \\ \nu \end{pmatrix}} \left[\mathbf{e}^\dagger \begin{pmatrix} \mathbf{q} \\ \nu \end{pmatrix} \frac{\partial \mathbf{D}(\mathbf{q})}{\partial q_\alpha} \mathbf{e} \begin{pmatrix} \mathbf{q} \\ \nu \end{pmatrix} \right], \quad (21)$$

where the superscript \dagger denotes the conjugate transpose. In this case, a finite difference is applied to approximate the derivative of the dynamical matrix with respect to the wave vector components. The issues involved with the finite differencing of the frequency in Eq. (20) are no longer present. We recommend the use of Eq. (21).

A mode's Grüneisen parameter is a measure of its anharmonicity and plays a role in theory related to thermal expansion. It is defined for a cubically isotropic system as

$$\gamma \begin{pmatrix} \mathbf{q} \\ \nu \end{pmatrix} = -\frac{V}{\omega \begin{pmatrix} \mathbf{q} \\ \nu \end{pmatrix}} \frac{d\omega \begin{pmatrix} \mathbf{q} \\ \nu \end{pmatrix}}{dV}. \quad (22)$$

The mode Grüneisen parameter can be evaluated by performing a harmonic lattice dynamics calculation over a range of volumes around the equilibrium state and using a finite difference to approximate the derivative. The Grüneisen parameter can also be calculated without any approximation using the cubic force constants.⁶³ Such a calculation provides a check on a force constant calculation implementation. The bulk

Grüneisen parameter is given by

$$\gamma = \frac{\sum_{\mathbf{q},\nu} c\left(\frac{\mathbf{q}}{\nu}\right) \gamma\left(\frac{\mathbf{q}}{\nu}\right)}{\sum_{\mathbf{q},\nu} c\left(\frac{\mathbf{q}}{\nu}\right)}. \quad (23)$$

For non-cubic materials, the mode-dependent and bulk Grüneisen parameters are tensors.⁶⁴

C. Implementation

It is straightforward to write a computer program to perform harmonic lattice dynamics and to calculate the associated mode- and system-level phonon properties. Ideally, the program should be decoupled from the calculation of the harmonic force constants, which may come from an empirical potential or from DFT. The General Utility Lattice Package (GULP) can perform a wide variety of calculations related to harmonic lattice dynamics.⁶⁵

As discussed in Sec. III C 4, the force, harmonic, and cubic cutoffs must be specified when calculating force constants using finite displacements. When applying the finite difference method, we take the force and harmonic cutoffs to be the same. Analyzing how the force on an atom depends on its distance from the displaced atom provides a suggestion for the force cutoff (Fig. 3). We have found, however, that examining the dispersion curves provides better guidance for the selection of the harmonic cutoff.

As an example, consider the silicon [100] transverse acoustic dispersion curves plotted in Fig. 4. The finite difference curves correspond to a force/harmonic cutoff of 5-10 neighbor shells (5.4–7.5 Å) and are compared to a higher-accuracy DFPT prediction. Even at a cutoff of 10 neighbor shells, the finite difference prediction does not capture key features of the DFPT

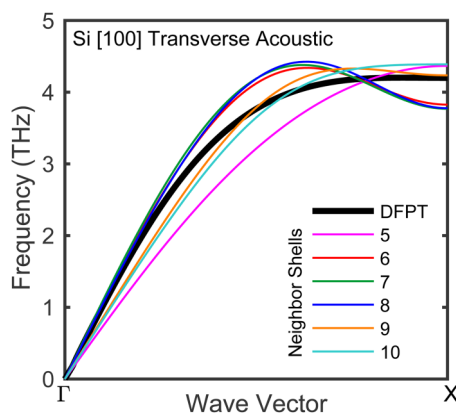


FIG. 4. Silicon [100] transverse acoustic dispersion curves calculated from (i) DFPT and (ii) finite differences using an increasing number of neighbor shells. Even at ten neighbor shells, the finite difference prediction does not match the higher accuracy of the DFPT result.

result, notably the slope at the Γ -point, which corresponds to the sound speed, and the frequency at the X-point. Mazur and Pollmann report a similar sensitivity of silicon's transverse acoustic branches to the number of neighbor shells considered in calculations based on a semi-empirical approach.⁶⁶ The longitudinal acoustic, transverse optical, and longitudinal optical dispersion curves predicted from finite differences show a smaller spread and better agreement with the DFPT predictions (see Figs. S1–S3 in the [supplementary material](#)).

We have found a similar behavior for other materials. That is, a large force/harmonic cutoff is required to obtain converged dispersion curves. In some cases, the dispersion curves are never satisfactory. The need to use large supercells adds significantly to the computational cost. For example, while a 216-atom supercell (i.e., three conventional unit cells in each direction) for silicon provides up to the tenth neighbor force constants, a 512-atom supercell (four conventional unit cells in each direction) is required to access the 11th to 17th neighbor shells (5.5–10.8 Å). As such, we typically perform DFPT calculations to obtain the harmonic force constants and recommend this practice.

V. BOLTZMANN TRANSPORT EQUATION

A. Intrinsic scattering

The harmonic lattice dynamics calculations described in Sec. IV provide the mode-dependent volumetric specific heats and group velocities needed to evaluate thermal conductivity from Eq. (5). The other required inputs are the lifetimes, $\tau_\alpha\left(\frac{\mathbf{q}}{\nu}\right)$, which are the focus of this section. Calculating the lifetimes requires anharmonic lattice dynamics, perturbation theory, and the BTE. The underlying theory and the associated computational implementation are significantly more challenging than harmonic lattice dynamics. Because packages are available that can provide the lifetimes (Sec. VIII), the majority of researchers are unlikely to develop their own codes. As such, we focus our attention on a high-level view of the theory, on understanding factors that may differentiate these packages, and on decisions that the user still needs to make. The reader is referred to previous works that describe the theory and implementation in detail.^{64,67–69}

The intrinsic phonon lifetimes (i.e., related to the scattering of phonons with other phonons) are calculated based on a perturbation to the non-interacting harmonic modes. As such, the wave vectors, frequencies, and eigenvectors obtained from harmonic lattice dynamics are required inputs to the calculation along with the atomic structure. The perturbation is realized through the inclusion of higher-order terms in the potential energy expansion given by Eq. (6). We focus our attention on the third-order term, which captures three-phonon interactions through the cubic force constants. Quartic effects (i.e., four-phonon interactions) are discussed in Sec. VI A. Extrinsic scattering is discussed in Sec. V C.

The intrinsic lifetime of mode $(\mathbf{q}, \nu)_1$ depends on all of its possible three-phonon interactions with other modes. Denoting two participating modes as $(\mathbf{q}, \nu)_2$ and $(\mathbf{q}, \nu)_3$, such a three-phonon interaction can take on two forms. In a Type I interaction, (i) mode 1 creates modes 2 and 3 or (ii) modes 2 and 3 create mode 1. In a Type II interaction, (i) mode 1 combines with mode 2(3) to create mode 3(2) or (ii) mode 2(3) creates modes 1 and 3(2). The translation invariance of the crystal requires that

$$\mathbf{q}_1 = \mathbf{q}_2 + \mathbf{q}_3 + \mathbf{G} \text{ (Type I) ,} \quad (24)$$

$$\mathbf{q}_1 + \mathbf{q}_{2(3)} = \mathbf{q}_{3(2)} + \mathbf{G} \text{ (Type II) ,} \quad (25)$$

where \mathbf{G} is the zero vector (corresponding to a normal process) or a reciprocal lattice vector (corresponding to an Umklapp process).

The intrinsic scattering rate Ω for either a Type I or Type II interaction, where the initial state is denoted by i and the final state by f , is given by the Fermi golden rule as

$$\Omega_{i \rightarrow f} = \frac{2\pi}{\hbar} |\langle f | U_3 | i \rangle|^2 \delta(E_i - E_f), \quad (26)$$

where $\langle f | U_3 | i \rangle$ is the matrix element of U_3 [the third order term in Eq. (6)] between the initial and final states. $\delta(E_i - E_f)$ is a delta function that ensures conservation of energy, E , i.e., $E_i = E_f$, such that

$$\hbar\omega_1 = \hbar\omega_2 + \hbar\omega_3 \text{ (Type I) ,} \quad (27)$$

$$\hbar\omega_1 + \hbar\omega_{2(3)} = \hbar\omega_{3(2)} \text{ (Type II) .} \quad (28)$$

Equations (24), (25), (27), and (28) provide information about the allowed three-phonon interactions. They can be used to quantify the phase space available to one mode (which is also known as the joint density of states or the two-phonon density of states) and to the entire system.⁷⁰ These phase space measures can be weighted by the Bose-Einstein distribution to include the effect of temperature. Because the cubic force constants are not used, the phase space measures do not provide information about the strengths of the interactions.

Evaluating the matrix elements in Eq. (26) requires

- the mode wave vectors, frequencies, and eigenvectors obtained from harmonic lattice dynamics (Sec. IV),
- the cubic force constants (Sec. III),
- the mode populations, which are obtained by solving the BTE as described below.

A mode's scattering rates for all Type I and II interactions are then combined to give its lifetime, $\tau_\alpha(\mathbf{q}, \nu)$. At this point, thermal conductivity can be obtained from Eq. (5).

The BTE is solved to determine the mode populations. Under the RTA, the populations are assumed to follow their equilibrium distribution (i.e., BE for a quantum system or

Boltzmann for a classical system). Calculation of the lifetimes under the RTA, which are known as the relaxation times $\tau_{\text{RTA}}(\mathbf{q}, \nu)$, is reasonably straightforward.⁷¹

The central assumption underlying the RTA is that both normal and Umklapp process are resistive and return a mode's population to the equilibrium distribution. Normal processes are, in fact, not resistive and return the population to a displaced distribution. When normal processes are important (e.g., at low temperatures and/or in high thermal conductivity materials), the RTA can lead to significant underprediction of thermal conductivity.^{12,72} In these cases, the BTE must be solved for the non-equilibrium populations. A variety of approaches have been developed, which include iterative,²⁶ variational,²⁷ and direct²⁸ solutions. The iterative and variation solutions both start from the RTA and all three solutions should produce the same set of non-equilibrium populations. It is not typically known *a priori* if the BTE solution is required or if the RTA is sufficient. The intrinsic phonon lifetimes obtained from the BTE solution are direction-dependent and can be negative. Such a result is possible because the quantities being solved for are the phonon populations and their deviation from equilibrium.

The phonon modes are a coordinate transform of the atomic positions. They correspond to the eigenvalues and eigenvectors of the dynamical matrix. Cepellotti and Marzari suggest an alternative transformation based on the eigenvalues and eigenvectors of the collision term in the BTE [Eq. (2)].^{73,74} The resulting energy carriers, which they call relaxons, are superpositions of phonon modes. Relaxons always decay to their equilibrium distribution and have well-defined relaxation times and mean free paths. When the RTA is valid, the phonon modes and relaxon modes are essentially the same. However, when the RTA is not valid, relaxons provide a convenient and intuitive way to interpret thermal transport.

B. Phonon mean free path

The phonon mean free path (MFP) is the average distance a phonon travels between scattering events. Under the RTA, the intrinsic MFP is thus

$$\Lambda_{\text{RTA}} \left(\begin{matrix} \mathbf{q} \\ \nu \end{matrix} \right) = \left| \mathbf{v}_g \left(\begin{matrix} \mathbf{q} \\ \nu \end{matrix} \right) \right| \tau_{\text{RTA}} \left(\begin{matrix} \mathbf{q} \\ \nu \end{matrix} \right). \quad (29)$$

Due to the directional dependence of the phonon lifetimes obtained from the BTE solution, however, the definition of the MFP becomes ambiguous.

We are aware of two methods for calculating a MFP from the BTE solution. In the ShengBTE package,³² the components of the mean free displacement vector $\mathbf{F}(\mathbf{q}, \nu)$ vector are defined as

$$F_\alpha \left(\begin{matrix} \mathbf{q} \\ \nu \end{matrix} \right) = v_{g,\alpha} \left(\begin{matrix} \mathbf{q} \\ \nu \end{matrix} \right) \tau_\alpha \left(\begin{matrix} \mathbf{q} \\ \nu \end{matrix} \right). \quad (30)$$

The MFP is then defined as the scalar projection of the mean

free displacement onto the group velocity vector, resulting in

$$\Lambda\left(\mathbf{q}_\nu\right)=\frac{\mathbf{F}\left(\mathbf{q}_\nu\right) \cdot \mathbf{v}_g\left(\mathbf{q}_\nu\right)}{\left|\mathbf{v}_g\left(\mathbf{q}_\nu\right)\right|} . \quad (31)$$

A second method, which we have used in our previous work,^{51,75,76} is to use the lifetime corresponding to the direction of the applied heat flow in the BTE solution for the MFP calculation. For heat flow in the α -direction, this formulation results in

$$\Lambda\left(\mathbf{q}_\nu\right)=\left|\mathbf{v}_g\left(\mathbf{q}_\nu\right)\right| \tau_\alpha\left(\mathbf{q}_\nu\right) . \quad (32)$$

C. Extrinsic scattering

1. Combining scattering mechanisms

A phonon will scatter due to any disruption to the atomic periodicity. The three-phonon interactions described in Sec. V A occur because atoms vibrate at finite temperature. Extrinsic factors can also scatter phonons and should be included in the calculation of a mode's lifetime. Scattering mechanisms can be combined in two ways.

First, all scattering mechanisms, intrinsic and extrinsic and indexed by i , are assumed to be independent and are combined using the Matthiessen rule as^{77,78}

$$\frac{1}{\tau\left(\mathbf{q}_\nu\right)}=\sum_i \frac{1}{\tau_i\left(\mathbf{q}_\nu\right)} . \quad (33)$$

This approach can be used with intrinsic lifetimes obtained from the RTA or the BTE solution. The applicability of the Matthiessen rule as related to intrinsic, phonon-boundary, and phonon-isotope scattering has been investigated. Luisier found that the Matthiessen rule overestimated the thermal conductivity of roughened silicon nanowires due to an additional scattering contribution of localized surface modes coupled to phonon-phonon scattering.⁷⁹ Similarly, Feng *et al.* reported an overestimation of thermal conductivity calculated by the Matthiessen rule in bulk silicon that resulted from a failure to account for coupling between impurity and phonon-phonon scattering.⁸⁰

Second, by self-consistently solving the BTE so that the non-equilibrium populations reflect all scattering mechanisms.⁵⁷ We have found that including phonon-boundary scattering in this manner can help with the convergence of the iterative solution of the BTE for graphene.

2. Phonon-defect scattering

Theory for phonon scattering by a mass defect (i.e., an isotope) was developed by Tamura using perturbation theory.⁸¹ The formulation is based on an assumption of elastic scattering, whereby the incident and created phonons have

the same frequency. The inputs to the calculation are the unit cell, the isotopic masses and concentrations, and the mode frequencies, eigenvectors, and populations. Energy conservation is satisfied using a delta function (see Sec. V D 2). This formulation can also be applied to alloys, as discussed in Sec. VI C. Theory for scattering by other point defects (e.g., vacancies, impurities, antisites, small clusters)^{82–84} and dislocations^{85,86} is emerging.

3. Phonon-electron scattering

Phonon-electron scattering is important in strongly-doped semiconductors.^{87,88} The details of calculating the associated lifetimes, which require phonon-electron coupling coefficients, are beyond the scope of this tutorial and can be found elsewhere.^{89,90} The electron-phonon Wannier package is useful for performing calculations related to phonon-electron interactions.⁹¹

Thermal conduction in a metal is due to phonons and electrons. The phonon contribution can be predicted using the tools described herein by including both phonon-phonon and phonon-electron scattering.^{92,93} The electronic contribution to thermal conductivity as well as the electrical conductivity and Seebeck coefficient can be obtained by solving the electronic BTE and using the Onsager relations.^{90,92} These calculations require the electron transport relaxation time, which is limited by phonon-electron scattering at temperatures ~ 100 -500 K for many metals. Electron-impurity and electron-electron scattering may become important outside of this range.

4. Phonon-boundary scattering

Phonon-boundary scattering in a nanostructure is the origin of its reduced thermal conductivity. It is characterized by the lifetime

$$\tau_b\left(\mathbf{q}_\nu\right)=\frac{\Lambda_b\left(\mathbf{q}_\nu\right)}{\left|\mathbf{v}_g\left(\mathbf{q}_\nu\right)\right|} , \quad (34)$$

where $\Lambda_b\left(\mathbf{q}_\nu\right)$ is the boundary scattering MFP, which is the average distance the phonon travels ballistically after its creation before hitting a system boundary. The phonon-boundary lifetime can be used in the Matthiessen rule or in the BTE solution. The boundary scattering MFP can be obtained analytically for simple geometries by an integration over all possible starting points for a phonon.⁹⁴ For a film of thickness L oriented such that the cross-plane direction is z with diffuse phonon-boundary scattering, it is given by

$$\Lambda_{b,\text{film}}\left(\mathbf{q}_\nu\right)=\frac{L}{2}\left|\frac{\mathbf{v}_g\left(\mathbf{q}_\nu\right)}{v_{g,z}\left(\mathbf{q}_\nu\right)}\right| . \quad (35)$$

For a wire of diameter D whose axis is oriented along the

z-direction with diffuse phonon-boundary scattering,

$$\Lambda_{b,wire}(\mathbf{q}_\nu) = \frac{4D}{3\pi} \left| \frac{\mathbf{v}_g(\mathbf{q}_\nu)}{\sqrt{v_{g,x}^2(\mathbf{q}_\nu) + v_{g,y}^2(\mathbf{q}_\nu)}} \right|. \quad (36)$$

The effect of a partially specular surface can also be included in the calculations. For more complicated geometries where an analytical solution is not possible (e.g., a thin film with a periodic array of pores), ballistic ray-tracing techniques can be applied.^{76,95} The use of a single boundary scattering MFP for a spectrum of phonons, as results from a Casimir limit calculation,^{78,96} is based on an integration over all propagation directions and an assumption that all phonons originate at a boundary (i.e., it represents purely ballistic transport).

Phonon-phonon and phonon-boundary scattering can be combined without the Matthiessen rule by using the free path sampling technique.^{76,97,98} Free path sampling takes the group velocity vectors and the intrinsic mean free paths as input and calculates effective mean free paths based on the geometry of the structure. For each phonon mode, an ensemble of free paths are sampled from a Poisson distribution. Each phonon is started from a random position inside the structure. The phonon is traced from its origin in the direction of its group velocity vector until it either reaches the end of its free path or it encounters a boundary. If the phonon encounters a boundary, its free path is truncated as the distance from its origin to the boundary; otherwise, the free path remains the same. After all the free paths are found, they are averaged to provide the effective mean free path, which contains information from both intrinsic scattering and geometry-specific boundary scattering. This formulation is in contrast to ray-tracing techniques, where the scattering rates are calculated separately and then combined using the Matthiessen rule. In this way, free path sampling avoids the assumption of independent scattering mechanisms as changes to the intrinsic mean free path change the boundary scattering rate and vice versa.

D. Implementation

1. Cubic force constant cutoff

The scattering rate calculation is expensive and strongly depends on the number of cubic force constants used, which is set by the cubic cutoff (Sec. III C 4). Cubic force constants are typically much shorter range than harmonic force constants. As described in Sec. VII B, we set the cubic cutoff by examining the thermal conductivity convergence.

2. Identifying three-phonon scattering events

It is computationally efficient to identify the three-phonon phase space (i.e., the sets of three modes that satisfy the translation invariance and energy conservation constraints) before calculating the scattering rates. Any calculation of phonon properties is made on a wave vector grid of finite

(and typically uniform) resolution. While it is straightforward to exactly satisfy translation invariance, the conservation of energy constraint requires careful attention. Three techniques have been developed for handling this challenge.

The first technique is to approximate the energy conservation delta function using a Gaussian or Lorentzian function of fixed width for all three-phonon interactions. When the width is small, few processes satisfy energy conservation, but the contribution from each of these processes is high. As the width is increased, more processes satisfy energy conservation, but the contribution from each process decreases. There is thus an optimal width that gives a meaningful value of the scattering rate.³²

The second technique is to use adaptive broadening, where the delta function is approximated by^{71,99}

$$\delta(\omega) \approx \frac{1}{\pi} \frac{\epsilon}{\omega^2 + \epsilon^2}, \quad (37)$$

where ϵ is the broadening parameter and is calculated as

$$\epsilon = \frac{1}{2} \left[\frac{1}{\tau(\mathbf{q}_\nu)_1} + \frac{1}{\tau(\mathbf{q}_\nu)_2} + \frac{1}{\tau(\mathbf{q}_\nu)_3} \right]. \quad (38)$$

The delta function is satisfied by providing an initial guess for the broadening parameter and iterating on the lifetimes until self-consistency is achieved in the RTA step. This broadening parameter is kept fixed during the BTE solution.

The third approach is to satisfy energy conservation exactly based on an interpolation scheme on a tetrahedral grid.^{68,100} This approach is computationally cheaper than the two broadening approaches but is more challenging to implement.

3. Thermal conductivity convergence with phonon wave vector grid

Putting aside for now decisions related to the DFT, force constant, and harmonic lattice dynamics calculations, the phonon wave vector grid must be varied in order to predict a resolution-independent thermal conductivity. The general practice is to increase the grid resolution (and thus the number of wave vectors) and observe the behavior of the thermal conductivity. For a cubic system, the wave vector resolution should be the same in the q_x , q_y , and q_z directions. For non-cubic systems, we recommend specifying the resolution such that the volume associated with each wave vector is a cube.

Three behaviors are possible for how thermal conductivity changes with increasing the wave vector resolution. They are related to the complex interplay between the contribution of modes near the Γ -point and the allowed three-phonon interactions. First, thermal conductivity converges to a resolution-independent value, as shown in Sec. VII for silicon. Second, thermal conductivity increases as the resolution increases.^{17,71} Third, thermal conductivity decreases as the resolution increases.¹⁰¹ Specification of thermal conductivity

in the first case is trivial. This situation is ideal and should be displayed in any material, given unlimited computational resources. Finite computational resources lead to the second and third cases. In these cases, an interpolation technique can be applied where the inverse of thermal conductivity is plotted versus the inverse of the wave vector resolution in one dimension. The data are fit to a line and extrapolated to the case of infinite resolution. It is not possible to know which of these three behaviors will be followed *a priori*.

E. Comparison of predictions and experimental measurements

Having laid out the procedure for predicting thermal conductivity, we now return to Fig. 1. Experimental measurements^{1–10} and theoretical predictions^{11–14} are plotted for a range of bulk crystalline materials between temperatures of 0 and 500 K. All experimental samples are naturally occurring (i.e., they contain isotopes) and this effect is included in the predictions for all materials except SrTiO₃ and PbTe. At a temperature of 300 K, the thermal conductivities range from 2 W/m K (PbTe) to 2000 W/m K (diamond) and the agreement between measurements and predictions is excellent.

The measurements all follow the same temperature-dependent trends. At low temperature, thermal conductivity increases with increasing temperature. Phonon transport in this regime is limited by boundary scattering due to the sample size, and the temperature dependence is related to the specific heat [Eqs. (18) and (19)], following a T^3 dependence. There is a maximum in thermal conductivity, followed by a decrease with increasing temperature. As temperature is increased, phonon populations increase according to Eq. (4), leading to increased intrinsic scattering. The thermal conductivity scaling beyond the maximum is typically T^{-m} , where $1 \leq m \leq 2$. Around the maximum, phonon transport is sensitive to defect scattering and the maximum thermal conductivity is strongly related to the sample purity.^{27,102} This effect can be seen in the GaN and SrTiO₃ data, where two sets of measurements are presented that agree at higher temperatures but diverge at lower temperatures.

All the predictions start at a temperature of 100 K, which is common across the available literature. Based on the discussion in the previous paragraph, we surmise that this minimum temperature is selected to ensure that the predictions correspond to a regime where intrinsic scattering dominates and defect scattering (here, dominated by isotopes) is a perturbation. Including isotopic scattering at these temperatures is critical for obtaining the excellent agreement realized between the measurements and predictions.^{11,12} In interpreting their predictions for SrTiO₃, where the agreement with the experimental data worsens as temperature decreases, Feng *et al.* argue that the presence of defects related to oxygen vacancies may lead to their overestimation of the measurements.¹³ For PbTe, isotope scattering was not included in the predictions of Shiga *et al.*¹⁴ It is likely not critical due to the low thermal conductivity and heavy atomic masses, such that the isotopic mass difference has a smaller

effect compared to the lighter atoms present in the higher thermal conductivity materials. Recent work by Xia that included four-phonon scattering (Sec. VI A) and renormalization (Sec. VI B) also found agreement with experimental measurements for PbTe.¹⁰³ This result suggests that the agreement found by Shiga *et al.*, who considered only three-phonon scattering and a zero-temperature structure, may be due to a cancelation of errors.

Many of the experimental data sets were obtained in the 1960s and terminate at a temperature of 300 K. There is a lack of high-quality bulk thermal conductivity measurements for many materials where phonons dominate thermal transport at higher temperatures. The maximum plotted temperature, 500 K, corresponds to the maximum temperature at which predictions are typically reported. Above this temperature, the assumptions of only including three-phonon scattering and a zero-temperature structure may break down. These effects are further discussed in Secs. VI A and VI B.

VI. ADVANCED TOPICS

A. Higher-order phonon processes

The discussion in Sec. V A was specific to intrinsic scattering events that involved three phonons. The Taylor series expansion of the potential energy in Eq. (6) is infinite, such that scattering events involving more than three phonons are possible. Recent work has identified the importance of four-phonon scattering in a range of materials.^{104–108} Their role can be assessed by comparing thermal conductivities to predictions from molecular dynamics simulations, which include the full anharmonicity of the atomic interactions, or to experimental measurements.

There are two general situations in which four-phonon scattering events are important: (i) When strong anharmonicity leads to large atomic displacements, such that atoms explore a large range of the potential energy surface. This situation is present in materials that are intrinsically strongly anharmonic [e.g., Lennard-Jones argon ($k \sim 0.1$ – 1 W/m K)¹⁰⁴ and NaCl ($k \sim 5$ W/m K at a temperature of 300 K)¹⁰⁷] and in all materials as temperature increases.^{104,105} (ii) When weak anharmonicity leads to low three-phonon scattering rates, such that the vast number of four-phonon scattering events makes them important. For example, inclusion of four-phonon scattering reduces the predicted thermal conduction of BAs at a temperature of 300 K from 2200 W/m K to 1400 W/m K,¹⁰⁵ bringing the prediction into agreement with experimental measurements.^{108–110} An even larger reduction has been predicted for single-layer graphene.¹⁰⁶

To include four-phonon scattering in the thermal conductivity prediction, a term is added to Eq. (26). As with three-phonon processes, the four phonons must satisfy constraints related to their wave vectors and energies. Calculation of the scattering rate requires the fourth-order (i.e., quartic) force constants. The BTE can be solved under the RTA or by solving for the non-equilibrium populations. The main challenge associated with including four-phonon scattering events is their sheer number.

B. Finite temperature effects

Finite temperature leads to anharmonicity, which has two effects: thermal expansion and atoms that no longer oscillate in a harmonic energy well. Thermal expansion can be captured with a quasi-harmonic calculation, where the finite temperature lattice constant is used in the harmonic framework. This calculation, however, cannot predict the vibrational structure of phases that are unstable at zero temperature (e.g., the tetragonal and pseudo-cubic phases of the lead halide perovskite MAPbI_3 ¹¹¹). Imaginary frequencies result, which indicate instability. This information is useful for understanding phase transitions but prevents calculation of phonon lifetimes and thermal conductivity.

The instability of the quasi-harmonic description of such systems is suppressed at finite temperature by anharmonicity. Finite-temperature force constants are thus required to obtain the true vibrational structure. One approach is to extract them from atomic configurations obtained from MD simulations.^{112–114} A recently proposed technique generates an ensemble of finite-temperature structures using a stochastic phase space sampling scheme,^{115,116} enabling the use of Bose-Einstein (i.e., quantum) statistics. Finite temperature force constants can also be obtained from self-consistent calculations.^{117,118}

Finite temperature also changes the phonon frequencies, which requires a renormalization of the phonon modes. The renormalization can be performed directly by calculating a frequency shift from the cubic and quartic force constants^{58,71,119} or by self-consistently correcting the dynamical matrix such that corrections are propagated in both the frequencies and eigenvectors.¹⁰⁷

C. Alloys

The discussion to this point has focused on predicting the thermal conductivity of a perfect crystal that may contain defects and/or be of finite size. The thermal conductivity prediction workflow can also be applied to alloys, where the atomic positions follow a lattice structure, but the constituent species are spatially random. That is, alloys are structurally ordered but compositionally disordered. The approach is to model the alloy as a virtual crystal with the disorder included as a perturbation.

The compositional disorder in an alloy is manifested in the atomic masses and force constants. The virtual crystal averages over these properties. First, consider the mass. In $\text{Si}_x\text{Ge}_{1-x}$, the virtual crystal contains one species with a mass equal to the average of that in the alloy. For $\text{In}_{1-x}\text{Ga}_x\text{As}$, the virtual crystal contains two species: one that averages over the In and Ga atoms and the periodic As atoms as the other. The simplest approach for the force constants is to average those of the two associate bulk phases based on the composition. This approach can be applied with DFT or an empirical potential. A better approach in DFT is to mix the pseudopotentials and then calculate the force constants.

The phonon-phonon scattering rates for the virtual crystal are then calculated as described in Sec. V A. The effect of the mass disorder is included using the theory developed

for phonon-isotope scattering described in Sec. V C 2. This approach has successfully predicted thermal conductivity measurements for $\text{Si}_{1-x}\text{Ge}_x$ ¹²⁰ and $\text{Mg}_2\text{Si}_{1-x}\text{Sn}_x$ alloys.⁵⁷ In $\text{PbTe}_{1-x}\text{Se}_x$ ¹²¹ and $\text{In}_{1-x}\text{Ga}_x\text{As}$ ¹²² alloys, however, an additional perturbation due to local variations in the force constants is required.¹²²

The workflow cannot be applied to amorphous materials, which have long-range structural disorder such that it is not possible to define a unit cell. A harmonic lattice dynamics calculation can be applied by treating the computational cell as the unit cell and performing a Γ -point calculation.¹²³ This calculation, which imposes a periodicity, provides mode frequencies and eigenvectors. With sufficient computational resources, the phonon lifetimes could also be extracted, but such a calculation seems impractical at this time. Because of the symmetry around the Γ -point, however, all modes will have zero group velocity (other than the three acoustic modes) such that a thermal conductivity prediction is not possible.

VII. CASE STUDY: SILICON

A. Benchmark

Many choices need to be made as part of a thermal conductivity prediction. These choices are related to the DFT calculations, the force constant calculations, the harmonic lattice dynamics calculations, and the BTE solution. In this section, we provide benchmarking data for a case study on isotopically pure silicon. In Sec. VII B, a series of convergence tests on this system are presented. The DFT and DFPT calculations are performed with Quantum Espresso³⁷ version 6.0 using the norm-conserving pseudopotential Si.pz-vbc.UPF and the LDA exchange-correlation functional. The lattice dynamics calculations and BTE solution are performed using an in-house code.

For the DFPT benchmark, the electronic wave vector grid is $8 \times 8 \times 8$ and the plane wave energy cutoff is 60 Ry. The minimum energy configuration of the two-atom face-centered cubic diamond structure is required to specify the zero-pressure lattice constant. It can be obtained using Quantum Espresso's built-in relaxation module. It can also be obtained by performing single-point energy calculations around a known starting point (e.g., the experimental lattice constant). A polynomial is fit to the resulting energies, whose minimum corresponds to the relaxed structure. Data generated using this approach are plotted in Fig. 5. A cubic fit to these data gives a lattice constant of 5.4018 Å.

Dynamical matrices are then obtained from DFPT calculations. We used a phonon wave vector grid of $8 \times 8 \times 8$ and a self-consistency threshold of 10^{-14} . The dynamical matrices are then mapped to the real-space harmonic force constants by a Fourier transform, and the phonon frequencies are obtained from harmonic lattice dynamics calculations. The resulting dispersion along high-symmetry directions is plotted in Fig. 6. The 6×6 dynamical matrices and frequencies for the Γ , X, W, and L points are provided in Sec. S2 of the [supplementary material](#).

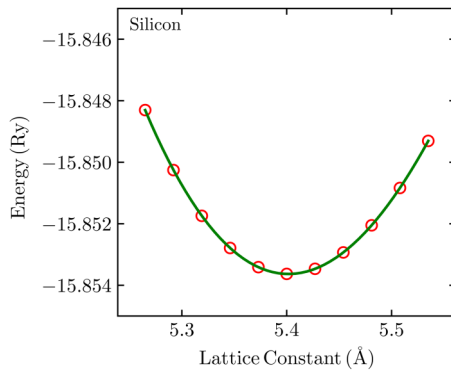


FIG. 5. Variation of DFT energy for silicon versus lattice constant (circles) and a cubic fit to the data (line). The minimum energy corresponds to the zero-pressure lattice constant.

For the anharmonic lattice dynamics calculations, the cubic cutoff was set at 4.86 \AA , corresponding to atoms up to and including the third neighbor shell. A set of displacements of size $h = 0.027 \text{ \AA}$ were applied to atoms in twenty-four $3 \times 3 \times 3$ supercells generated based on the crystal symmetries. The forces were calculated from DFT using a $1 \times 1 \times 1$ electronic wave vector grid on the atoms of interest. The cubic force constants were then extracted using finite differences [Eq. (14)]. Translational invariance was satisfied using a Lagrangian approach.⁵⁷ Energy conservation for three-phonon scattering events was satisfied using adaptive broadening [Eq. (38)]. For a phonon wave-vector grid size of $24 \times 24 \times 24$, the resulting thermal conductivity at a temperature of 300 K is 148 W/mK from the RTA solution and 152 W/mK from the iterative solution of the BTE. The thermal conductivity accumulation functions under the RTA and iterative solutions are

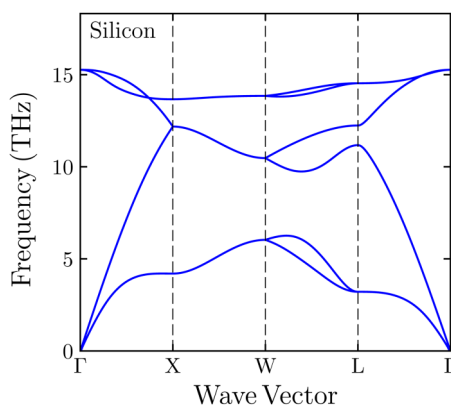


FIG. 6. Silicon dispersion along high-symmetry directions from DFPT and harmonic lattice dynamics calculations. The lattice constant is 5.4018 \AA . When scaled by the distance between Γ and X, $\Gamma = (0, 0, 0)$, $X = (1, 0, 0)$, $W = (1, 0.5, 0)$, and $L = (0.5, 0.5, 0.5)$.

TABLE III. Zero-pressure lattice constant (\AA) as a function of electronic wave vector grid and plane wave energy cutoff. The values used for the case study are $8 \times 8 \times 8$ and 60 Ry and the corresponding lattice constant is in bold.

	20 Ry	30 Ry	40 Ry	50 Ry	60 Ry	70 Ry	80 Ry
$2 \times 2 \times 2$	5.5486	5.5395	5.5398	5.5398	5.5399	5.5399	5.5399
$4 \times 4 \times 4$	5.4152	5.4136	5.4128	5.4129	5.4129	5.4129	5.4129
$6 \times 6 \times 6$	5.4059	5.4036	5.4029	5.4030	5.4030	5.4030	5.4030
$8 \times 8 \times 8$	5.4044	5.4024	5.4017	5.4018	5.4018	5.4018	5.4018
$10 \times 10 \times 10$	5.4044	5.4023	5.4016	5.4017	5.4017	5.4017	5.4017
$12 \times 12 \times 12$	5.4047	5.4024	5.4016	5.4017	5.4017	5.4017	5.4017

plotted in Fig. S4 as a function of MFP. The accumulations resulting from the two definitions of the MFP for the BTE solution, Eqs. (31) and (32), are indistinguishable. This result should not be taken as universal, however, as deviations may emerge in situations where the RTA is a poor assumption and/or the material is not isotropic.

B. Convergence

In this section, we present results from convergence tests performed on the isotopically pure silicon case study from Sec. VII A. Unless noted, the calculation parameters are the same as those from the case study.

To set the electronic wave vector grid and the plane wave energy cutoff, the zero-pressure lattice constant for different combinations of these two parameters was calculated. The results are provided in Table III. Convergence to within 0.0002 \AA is obtained for an electronic wave vector grid of $8 \times 8 \times 8$ and a plane wave energy cutoff of 60 Ry. These values provide a starting point for the ensuing calculations. Once the thermal conductivity has been predicted, a further convergence study starting from these values should be performed to ensure that the thermal conductivity is also converged for these two parameters.⁵¹

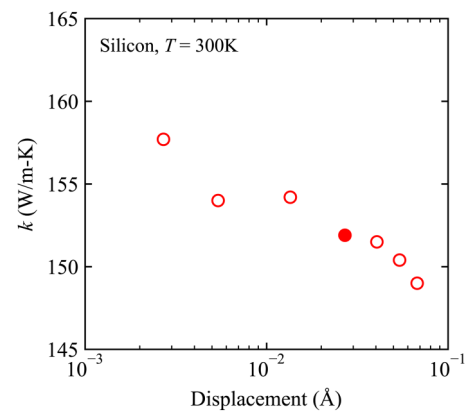


FIG. 7. Silicon thermal conductivity at a temperature of 300 K plotted as a function of the displacement size used when extracting the cubic force constants. The value used for the case study is 0.027 \AA and the corresponding marker is filled.

TABLE IV. Number of displaced structures and resulting thermal conductivity for different choices of the cubic cutoff. Three neighbor shells are used for the case study and the corresponding row is in bold.

Cubic cutoff [neighbor shells/distance (Å)]	# of displaced structures	k (W/m K) at $T = 300$ K
2/4.11	24	150
3/4.86	24	152
4/5.64	32	155
5/6.21	40	151
6/6.75	72	149

The effect of the atomic displacement size, h , on thermal conductivity is plotted in Fig. 7. The thermal conductivity is reasonably invariant for displacements between 0.004 and 0.04 Å.

The cubic cutoff sets the number of cubic force constants and the number of supercell structures. The effect of the cubic cutoff on the thermal conductivity predicted from the iterative solution of the BTE is shown in Table IV. The thermal conductivity predicted for a $2 \times 2 \times 2$ supercell is 153 W/m K and that for a $3 \times 3 \times 3$ supercell is 152 W/m K. The thermal conductivities predicted using Lagrangian⁵⁷ and uniform correction methods to satisfy translation invariance are both 152 W/m K. The variation of thermal conductivity with the phonon wave vector grid resolution is plotted in Fig. 8. The thermal conductivity is reasonably converged by $24 \times 24 \times 24$.

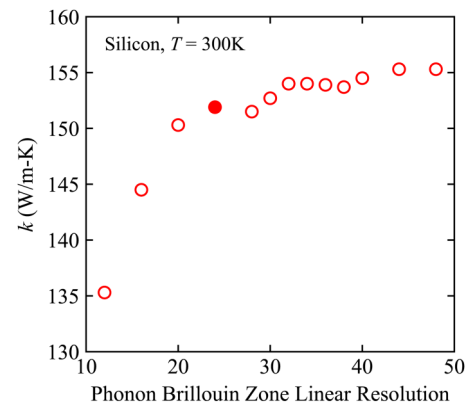


FIG. 8. Silicon thermal conductivity at a temperature of 300 K plotted as a function of the number of phonon wave vectors in each direction of the Brillouin zone. The value used for the case study is $24 \times 24 \times 24$ and the corresponding marker is filled.

VIII. COMPUTATIONAL PACKAGES

There are many packages available that can predict phonon properties and thermal conductivity using force constants obtained from DFT calculations. These include ALAMODE,²⁹ almaBTE,³⁰ phono3py,³¹ and ShengBTE.³² The main and differentiating features of these four packages are provided in Table V.

TABLE V. Features and capabilities of computational packages for predicting phonon properties and thermal conductivity. All of these packages use permutation and space group symmetries to reduce the number of distinct force constants, can handle long-range interactions, treat phonon-isotope scattering using Tamura's formulation,⁸¹ and provide mode-dependent Grüneisen parameters, the three-phonon phase space (modal and total), and the spectral thermal conductivity.

	ShengBTE ³²	almaBTE ³⁰	phono3py ³¹	ALAMODE ²⁹
BTE solution method	Iterative, RTA	Direct, Iterative, RTA	Direct, RTA	RTA
Harmonic force constant	DFPT, finite difference	DFPT, finite difference	Finite difference	Linear least-squares fitting
Cubic force constant	Finite difference	Finite difference	Finite difference	Linear least-squares fitting
Boundary scattering	Iterative for nanowire	Suppression function for thin film under RTA	Matthiessen rule with $\tau_b^{-1} = \mathbf{v}_g /L_c$ under RTA ^a	Matthiessen rule with $\tau_b^{-1} = 2 \mathbf{v}_g /L_c$ under RTA ^a
Frequency shift for cubic interaction	No	No	No	Yes
Quartic interactions	No	No	No	Frequency shift
MFP calculation	Eq. (31)	Eq. (31)	Eq. (29)	Eq. (29)
Translational invariance	Lagrangian ⁵⁷	Lagrangian ⁵⁷	Uniform correction ¹²⁴	LSE ^{125,b}
Energy conservation δ -function	Gaussian (adaptive)	Gaussian (adaptive)	Gaussian (fixed) or tetrahedron	Gaussian (fixed) or Lorentzian (fixed) or tetrahedron
DFT compatibility	QE, ^c VASP	VASP	ABINIT, CRYSTAL, ¹²⁶ QE, VASP	QE, VASP, xTAPP ^{127,128}
LAMMPS ^{129,d} Compatibility	No	No	No	Yes
Empirical potential compatibility	No	No	No	Yes
Unique outputs		Superlattice phonon properties		Mean square displacement

^a L_c is a characteristic length specific by the user.

^bLeast squares error.

^cQuantum ESPRESSO.

^dLarge-scale Atomic/Molecular Massively Parallel Simulator.

IX. SUMMARY AND OUTLOOK

In this tutorial, we described a computational framework for predicting the phonon contribution to the thermal conductivity of a crystalline solid (Fig. 2). Details related to the underlying theory and computational implementation were presented as a means to help researchers who are using available packages and developing their own codes.

There are many decisions to be made in a thermal conductivity prediction. The specification of parameters such as the electronic and phonon wave vector grids, the plane wave energy cutoff, the supercell size, the force constant cutoffs, and the atomic displacement size can all be checked through convergence studies, which will provide an associated uncertainty. Our experience is that, while results for other materials can provide guidance in these choices, every material behaves differently. It is critical to ensure convergence at all stages of the framework, from the lattice constant (Table III) to the dispersion (Fig. 4) to the thermal conductivity (Fig. 8). In the end, one seeks a balance between accuracy and computational cost.

The selections of the pseudopotential and exchange correlation functional used in the DFT calculations are more ambiguous. In this case, approximations associated with their formulation is a potential source of error when comparing to experimental measurements. Performing the thermal conductivity prediction for different pseudopotentials and exchange correlation functionals is one way to assess this uncertainty.^{51–53} The GGA-based Bayesian error estimation functional (BEEF)^{130,131} includes an ensemble of exchange-correlation functionals that enables a systematic assessment of uncertainty in DFT calculations and may be useful in interpreting thermal conductivity predictions.¹³¹

The computational framework is also limited by its computational demands. The number of distinct force constant can become very large for unit cells that lack symmetry and/or have many atoms. Reducing the force constant cutoffs reduces cost but can impact the accuracy of the predictions. Including four-phonon scattering is also computationally demanding.

When comparing predictions to measurements, there are different reasons for a potential disagreement. As discussed above, the prediction may not be properly converged (which the user should be able to ensure), and there are inherent approximations associated with the DFT calculations and the solution framework (e.g., if four-phonon scattering and finite temperature effects are ignored). Furthermore, the quality of the sample used in the experiment may be unknown (e.g., as related to defects and doping), such that an accurate inclusion of extrinsic scattering mechanisms may be difficult. In some cases, thermal transport mechanisms may be present that are not well-represented by phonons. For example, a recent study of Ti_3VSe_4 measured a room temperature thermal conductivity as 0.30 W/m K while predicting a value of 0.16 W/m K .¹³² In such cases, theoretical and computational tools may be needed that include mechanisms associated with disordered materials^{133,134} or that do not make an assumption of the existence of phonons.¹³⁵

While the use of DFT and DFPT calculations to obtain the force constants is powerful, the importance of empirical potentials should not be overlooked. They allow for an essentially instantaneous calculation of the force constants. Efforts to optimize existing potentials for thermal transport (e.g., Tersoff and Brenner for carbon nanotubes and graphene¹³⁶) and the emergence of potentials based on advanced statistical algorithms¹³⁷ point to their continued importance in modeling studies.

In looking to the future of thermal conductivity prediction, important advances continue to be made, notably related to four-phonon scattering (Sec. VI A), finite-temperature effects (Sec. VI B), and defect scattering (Sec. V C 2). For describing materials where phonons are not the only significant carriers of heat, thermal transport by electrons and magnons¹³⁸ must also be included. Finally, while many of the tools are in place, a rigorous computational framework for predicting interface thermal conductances that agree with experimental measurements has yet to be realized.

SUPPLEMENTARY MATERIAL

See [supplementary material](#) for longitudinal acoustic, transverse optical, and longitudinal optical dispersion curves for silicon from DFPT and finite differences; silicon dynamical matrices and frequencies at high-symmetry points; and the thermal conductivity accumulation function for silicon at a temperature of 300 K predicted by the RTA and BTE solutions.

ACKNOWLEDGMENTS

This work was supported by the National Science Foundation (NSF; Grant No. DMR-1507325) (A.J.H.M. and H.-Y.K.) and the China Scholarships Council (Award No. 201706280251) (B.F.). David Broido, Lucas Lindsay, Takuma Shiga, and Junichiro Shiomi provided some of the data used to make Fig. 1. Holden Parks provided the data used to make Figs. 4 and (S1)–(S3) in the [supplementary material](#) and gave helpful feedback.

REFERENCES

- ¹D. Greig, *Phys. Rev.* **120**, 358 (1960).
- ²M. Holland, *Phys. Rev.* **134**, A471 (1964).
- ³P. Maycock, *Solid State Electron.* **10**, 161 (1967).
- ⁴I. Yu, B. Ravich, and I. Smirnov, *Semiconducting Lead Chalcogenides* (Springer Science & Business Media, 1970).
- ⁵D. Morelli, J. Heremans, and G. Slack, *Phys. Rev. B* **66**, 195304 (2002).
- ⁶G. A. Slack, L. J. Schowalter, D. Morelli, and J. A. Freitas, Jr, *J. Cryst. Growth* **246**, 287 (2002).
- ⁷A. Jezowski, P. Stachowiak, T. Plackowski, T. Suski, S. Krukowski, M. Bockowski, I. Grzegory, B. Danilchenko, and T. Paszkiewicz, *Phys. Status Solidi B* **240**, 447 (2003).
- ⁸A. V. Inyushkin, A. N. Taldenkov, A. M. Gibin, A. V. Gusev, and H.-J. Pohl, *Phys. Status Solidi C* **1**, 2995 (2004).
- ⁹C. Yu, M. L. Scullin, M. Huijben, R. Ramesh, and A. Majumdar, *Appl. Phys. Lett.* **92**, 191911 (2008).
- ¹⁰M. T. Buscaglia, F. Maglia, U. Anselmi-Tamburini, D. Marré, I. Pallecchi, A. Ianculescu, G. Canu, M. Viviani, M. Fabrizio, and V. Buscaglia, *J. Eur. Ceram. Soc.* **34**, 307 (2014).
- ¹¹A. Ward, D. A. Broido, D. A. Stewart, and G. Deinzer, *Phys. Rev. B* **80**, 125203 (2009).

- ¹²L. Lindsay, D. A. Broido, and T. L. Reinecke, *Phys. Rev. B* **87**, 165201 (2013).
- ¹³L. Feng, T. Shiga, and J. Shiomi, *Appl. Phys. Exp.* **8**, 071501 (2015).
- ¹⁴T. Shiga, J. Shiomi, J. Ma, O. Delaire, T. Radzynski, A. Lusakovski, K. Esfarjani, and G. Chen, *Phys. Rev. B* **85**, 155203 (2012).
- ¹⁵J.-P. M. Péraud, C. D. Landon, and N. G. Hadjiconstantinou, *Annu. Rev. Heat Transfer* **17**, 205 (2014).
- ¹⁶D. A. Broido, M. Maloney, G. Birner, N. Mingo, and D. Stewart, *Appl. Phys. Lett.* **91**, 231922 (2007).
- ¹⁷K. Esfarjani, G. Chen, and H. T. Stokes, *Phys. Rev. B* **84**, 085204 (2011).
- ¹⁸K. Esfarjani, J. Garg, and G. Chen, *Annu. Rev. Heat Transfer* **17**, 9 (2014).
- ¹⁹L. Lindsay, *Nanoscale Microscale Thermophys. Eng.* **20**, 67 (2016).
- ²⁰S. Mohr, L. E. Ratcliff, L. Genovese, D. Caliste, P. Boulanger, S. Goedecker, and T. Deutsch, *Phys. Chem. Chem. Phys.* **17**, 31360 (2015).
- ²¹L. Lin, Z. Xu, and L. Ying, *Multiscale Model. Simul.* **15**, 29 (2017).
- ²²J. Che, T. Cagin, W. Deng, and W. A. Goddard III, *J. Chem. Phys.* **113**, 6888 (2000).
- ²³D. A. Broido, A. Ward, and N. Mingo, *Phys. Rev. B* **72**, 014308 (2005).
- ²⁴X. W. Zhou, S. Aubry, R. E. Jones, A. Greenstein, and P. K. Schelling, *Phys. Rev. B* **79**, 115201 (2009).
- ²⁵A. Debernardi, S. Baroni, and E. Molinari, *Phys. Rev. Lett.* **75**, 1819 (1995).
- ²⁶M. Omini and A. Sparavigna, *Phys. Rev. B* **53**, 9064 (1996).
- ²⁷G. Fugallo, M. Lazzeri, L. Paulatto, and F. Mauri, *Phys. Rev. B* **88**, 045430 (2013).
- ²⁸L. Chaput, *Phys. Rev. Lett.* **110**, 265506 (2013).
- ²⁹T. Tadano, Y. Gohda, and S. Tsuneyuki, *J. Phys. Condens. Matter* **26**, 225402 (2014).
- ³⁰J. Carrete, B. Vermeersch, A. Katre, A. van Roekeghem, T. Wang, G. K. Madsen, and N. Mingo, *Comput. Phys. Commun.* **220**, 351 (2017).
- ³¹A. Togo, L. Chaput, and I. Tanaka, *Phys. Rev. B* **91**, 094306 (2015).
- ³²W. Li, J. Carrete, N. A. Katcho, and N. Mingo, *Comput. Phys. Commun.* **185**, 1747 (2014).
- ³³D. Ellis, *Density Functional Theory of Molecules, Clusters, and Solids* (Springer Science & Business Media, 1995), Vol. 12.
- ³⁴D. S. Sholl and J. A. Steckel, *Density Functional Theory: A Practical Introduction* (Wiley, Hoboken, 2009).
- ³⁵S. Baroni, S. de Gironcoli, A. Dal Corso, and P. Giannozzi, *Rev. Mod. Phys.* **73**, 515 (2001).
- ³⁶R. Heid, *Emergent Phenomena in Correlated Matter: Autumn School Organized by the Forschungszentrum Jülich and the German Research School for Simulation Sciences at Forschungszentrum Jülich 23-27 September 2013*, Lecture Notes of the Autumn School Correlated Electrons Vol. 3 (German Research School for Simulation Sciences, 2013).
- ³⁷P. Giannozzi, S. Baroni, N. Bonini, M. Calandra, R. Car, C. Cavazzoni, D. Ceresoli, G. L. Chiarotti, M. Cococcioni, I. Dabo et al., *J. Phys. Condens. Matter* **21**, 395502 (2009).
- ³⁸J. J. Mortensen, L. B. Hansen, and K. W. Jacobsen, *Phys. Rev. B* **71**, 035109 (2005).
- ³⁹J. e. Enkovaara, C. Rostgaard, J. J. Mortensen, J. Chen, M. Dulak, L. Ferrighi, J. Gavnholt, C. Glinsvad, V. Haikola, H. Hansen et al., *J. Phys. Condens. Matter* **22**, 253202 (2010).
- ⁴⁰G. Kresse and J. Hafner, *Phys. Rev. B* **47**, 558 (1993).
- ⁴¹G. Kresse and J. Hafner, *Phys. Rev. B* **49**, 14251 (1994).
- ⁴²G. Kresse and J. Furthmüller, *Phys. Rev. B* **54**, 11169 (1996).
- ⁴³G. Kresse and J. Furthmüller, *Comput. Mater. Sci.* **6**, 15 (1996).
- ⁴⁴V. Blum, R. Gehrke, F. Hanke, P. Havu, V. Havu, X. Ren, K. Reuter, and M. Scheffler, *Comput. Phys. Commun.* **180**, 2175 (2009).
- ⁴⁵X. Gonze, F. Jollet, F. A. Araujo, D. Adams, B. Amadon, T. Applencourt, C. Audouze, J.-M. Beuken, J. Bieder, A. Bokhanchuk et al., *Comput. Phys. Commun.* **205**, 106 (2016).
- ⁴⁶A. H. Larsen, J. J. Mortensen, J. Blomqvist, I. E. Castelli, R. Christensen, M. Dulak, J. Friis, M. N. Groves, B. Hammer, C. Hargus et al., *J. Phys. Condens. Matter* **29**, 273002 (2017).
- ⁴⁷W. Kohn and L. J. Sham, *Phys. Rev.* **140**, A1133 (1965).
- ⁴⁸J. P. Perdew, J. A. Chevary, S. H. Vosko, K. A. Jackson, M. R. Pederson, D. J. Singh, and C. Fiolhais, *Phys. Rev. B* **46**, 6671 (1992).
- ⁴⁹J. P. Perdew, K. Burke, and M. Ernzerhof, *Phys. Rev. Lett.* **77**, 3865 (1996).
- ⁵⁰J. P. Perdew and K. Schmidt, *AIP Conf. Proc.* **577**, 1–20 (2001).
- ⁵¹A. Jain and A. J. H. McGaughey, *Comput. Mater. Sci.* **110**, 115 (2015).
- ⁵²G. Qin, Z. Qin, H. Wang, and M. Hu, *Comput. Mater. Sci.* **151**, 153 (2018).
- ⁵³A. Taheri, C. Da Silva, and C. H. Amon, *J. Appl. Phys.* **123**, 215105 (2018).
- ⁵⁴J. Kitchin, *Modeling Materials Using Density Functional Theory* (Free Software Foundation, Boston, 2008).
- ⁵⁵A. Togo and I. Tanaka, preprint [arXiv:1808.01590](https://arxiv.org/abs/1808.01590) (2018).
- ⁵⁶K. Esfarjani and H. T. Stokes, *Phys. Rev. B* **77**, 144112 (2008).
- ⁵⁷W. Li, L. Lindsay, D. A. Broido, D. A. Stewart, and N. Mingo, *Phys. Rev. B* **86**, 174307 (2012).
- ⁵⁸M. T. Dove, *Introduction to Lattice Dynamics* (Cambridge University Press, Cambridge, 1993).
- ⁵⁹A. J. H. McGaughey and J. M. Larkin, *Annu. Rev. Heat Transfer* **17**, 49 (2014).
- ⁶⁰H. J. Monkhorst and J. D. Pack, *Phys. Rev. B* **13**, 5188 (1976).
- ⁶¹D. A. McQuarrie, *Statistical Mechanics* (University Science Books, Sausalito, 2000).
- ⁶²J.-S. Wang, J. Wang, and J. T. Lü, *Eur. Phys. J. B* **62**, 381 (2008).
- ⁶³J. Fabian and P. B. Allen, *Phys. Rev. Lett.* **79**, 1885 (1997).
- ⁶⁴D. C. Wallace, *Thermodynamics of Crystals* (Cambridge University Press, Cambridge, UK, 1972).
- ⁶⁵J. D. Gale and A. L. Rohl, *Mol. Simul.* **29**, 291 (2003).
- ⁶⁶A. Mazur and J. Pollmann, *Phys. Rev. B* **39**, 5261 (1989).
- ⁶⁷J. A. Reissland, *The Physics of Phonons* (John Wiley and Sons Ltd, 1973).
- ⁶⁸A. Ward, Ph.D. thesis (Boston College, Boston, MA, 2009).
- ⁶⁹A. Jain, Ph.D. thesis (Carnegie Mellon University, Pittsburgh, PA, 2015).
- ⁷⁰L. Lindsay and D. A. Broido, *J. Phys. Condens. Matter* **20**, 165209 (2008).
- ⁷¹J. E. Turney, E. S. Landry, A. J. H. McGaughey, and C. H. Amon, *Phys. Rev. B* **79**, 064301 (2009).
- ⁷²L. Lindsay, D. A. Broido, and N. Mingo, *Phys. Rev. B* **82**, 115427 (2010).
- ⁷³A. Cepellotti and N. Marzari, *Phys. Rev. X* **6**, 041013 (2016).
- ⁷⁴A. Cepellotti and N. Marzari, *Nano Lett.* **17**, 4675 (2017).
- ⁷⁵W. Jin, P. Lu, and S. Li, *Sci. Rep.* **5**, 15640 (2015).
- ⁷⁶K. D. Parrish, J. R. Abel, A. Jain, J. A. Malen, and A. J. H. McGaughey, *J. Appl. Phys.* **122**, 125101 (2017).
- ⁷⁷A. Matthiessen and C. Vogt, *Philos. Trans. R. Soc. London* **154**, 167 (1864).
- ⁷⁸J. M. Ziman, *Electrons and Phonons* (Oxford, New York, 2001).
- ⁷⁹M. Luisier, *Appl. Phys. Lett.* **103**, 113103 (2013).
- ⁸⁰T. Feng, B. Qiu, and X. Ruan, *Phys. Rev. B* **92**, 235206 (2015).
- ⁸¹S. Tamura, *Phys. Rev. B* **27**, 858 (1983).
- ⁸²N. Mingo, K. Esfarjani, D. Broido, and D. Stewart, *Phys. Rev. B* **81**, 045408 (2010).
- ⁸³N. Katcho, J. Carrete, W. Li, and N. Mingo, *Phys. Rev. B* **90**, 094117 (2014).
- ⁸⁴A. Katre, J. Carrete, B. Dongre, G. K. Madsen, and N. Mingo, *Phys. Rev. Lett.* **119**, 075902 (2017).
- ⁸⁵M. Li, Z. Ding, Q. Meng, J. Zhou, Y. Zhu, H. Liu, M. S. Dresselhaus, and G. Chen, *Nano Lett.* **17**, 1587 (2017).
- ⁸⁶M. Li, Y. Tsurimaki, Q. Meng, N. Andrejevic, Y. Zhu, G. D. Mahan, and G. Chen, *New. J. Phys.* **20**, 023010 (2018).
- ⁸⁷B. Liao, B. Qiu, J. Zhou, S. Huberman, K. Esfarjani, and G. Chen, *Phys. Rev. Lett.* **114**, 115901 (2015).
- ⁸⁸T. E. Beechem, A. E. McDonald, E. J. Fuller, A. A. Talin, C. M. Rost, J.-P. Maria, J. T. Gaskins, P. E. Hopkins, and A. A. Allerman, *J. Appl. Phys.* **120**, 095104 (2016).
- ⁸⁹F. Giustino, M. L. Cohen, and S. G. Louie, *Phys. Rev. B* **76**, 165108 (2007).
- ⁹⁰G. D. Mahan, *Many-Particle Physics* (Springer Science & Business Media, 2013).
- ⁹¹S. Poncè, E. R. Margine, C. Verdi, and F. Giustino, *Comput. Phys. Commun.* **209**, 116 (2016).
- ⁹²A. Jain and A. J. H. McGaughey, *Phys. Rev. B* **93**, 081206 (2016).
- ⁹³Y. Wang, Z. Lu, and X. Ruan, *J. Appl. Phys.* **119**, 225109 (2016).
- ⁹⁴A. J. H. McGaughey, E. S. Landry, D. P. Sellan, and C. H. Amon, *Appl. Phys. Lett.* **99**, 131904 (2011).
- ⁹⁵T. Hori, J. Shiomi, and C. Dames, *Appl. Phys. Lett.* **106**, 171901 (2015).
- ⁹⁶H. Casimir, *Physica* **5**, 495 (1938).
- ⁹⁷A. J. H. McGaughey and A. Jain, *Appl. Phys. Lett.* **100**, 061911 (2012).
- ⁹⁸A. Jain, Y.-Y. Yu, and A. J. H. McGaughey, *Phys. Rev. B* **87**, 195301 (2013).

- ⁹⁹A. J. C. Ladd, B. Moran, and W. G. Hoover, *Phys. Rev. B* **34**, 5058 (1986).
- ¹⁰⁰P. E. Blöchl, O. Jepsen, and O. K. Andersen, *Phys. Rev. B* **49**, 16223 (1994).
- ¹⁰¹A. Jain and A. J. McGaughey, *J. Appl. Phys.* **116**, 073503 (2014).
- ¹⁰²M. Asen-Palmer, K. Bartkowski, E. Gmelin, M. Cardona, A. P. Zhernov, A. V. Inyushkin, A. Taldenkov, V. I. Ozhogin, K. M. Itoh, and E. E. Haller, *Phys. Rev. B* **56**, 9431 (1997).
- ¹⁰³Y. Xia, *Appl. Phys. Lett.* **113**, 073901 (2018).
- ¹⁰⁴T. Feng and X. Ruan, *Phys. Rev. B* **93**, 045202 (2016).
- ¹⁰⁵T. Feng, L. Lindsay, and X. Ruan, *Phys. Rev. B* **96**, 161201 (2017).
- ¹⁰⁶T. Feng and X. Ruan, *Phys. Rev. B* **97**, 045202 (2018).
- ¹⁰⁷N. K. Ravichandran and D. Broido, *Phys. Rev. B* **98**, 085205 (2018).
- ¹⁰⁸F. Tian, B. Song, X. Chen, N. K. Ravichandran, Y. Lv, K. Chen, S. Sullivan, J. Kim, Y. Zhou, T.-H. Liu *et al.*, *Science* **361**, 582 (2018).
- ¹⁰⁹J. S. Kang, M. Li, H. Wu, H. Nguyen, and Y. Hu, *Science* **361**, 575 (2018).
- ¹¹⁰S. Li, Q. Zheng, Y. Lv, X. Liu, X. Wang, P. Y. Huang, D. G. Cahill, and B. Lv, *Science* **361**, 579 (2018).
- ¹¹¹F. Brivio, J. M. Frost, J. M. Skelton, A. J. Jackson, O. J. Weber, M. T. Weller, A. R. Goni, A. M. Leguy, P. R. Barnes, and A. Walsh, *Phys. Rev. B* **92**, 144308 (2015).
- ¹¹²O. Hellman, I. Abrikosov, and S. Simak, *Phys. Rev. B* **84**, 180301 (2011).
- ¹¹³O. Hellman, P. Steneteg, I. A. Abrikosov, and S. I. Simak, *Phys. Rev. B* **87**, 104111 (2013).
- ¹¹⁴O. Hellman and I. A. Abrikosov, *Phys. Rev. B* **88**, 144301 (2013).
- ¹¹⁵N. Shulumba, O. Hellman, and A. J. Minnich, *Phys. Rev. B* **95**, 014302 (2017).
- ¹¹⁶N. Shulumba, O. Hellman, and A. J. Minnich, *Phys. Rev. Lett.* **119**, 185901 (2017).
- ¹¹⁷P. Souvatzis, O. Eriksson, M. Katsnelson, and S. Rudin, *Comput. Mater. Sci.* **44**, 888 (2009).
- ¹¹⁸T. Tadano and S. Tsuneyuki, *Phys. Rev. B* **92**, 054301 (2015).
- ¹¹⁹T. Feng, X. Yang, and X. Ruan, *J. Appl. Phys.* **124**, 145101 (2018).
- ¹²⁰J. Garg, N. Bonini, B. Kozinsky, and N. Marzari, *Phys. Rev. Lett.* **106**, 045901 (2011).
- ¹²¹T. Murakami, T. Shiga, T. Hori, K. Esfarjani, and J. Shiomi, *EPL (Europhys. Lett.)* **102**, 46002 (2013).
- ¹²²M. Arrigoni, J. Carrete, N. Mingo, and G. K. H. Madsen, *Phys. Rev. B* **98**, 115205 (2018).
- ¹²³J. M. Larkin and A. J. McGaughey, *Phys. Rev. B* **89**, 144303 (2014).
- ¹²⁴A. Togo, personal communication (2018).
- ¹²⁵T. Tadano and S. Tsuneyuki, *J. Phys. Soc. Jpn.* **87**, 041015 (2018).
- ¹²⁶R. Dovesi, A. Erba, R. Orlando, C. M. Zicovich-Wilson, B. Civalleri, L. Maschio, M. Rérat, S. Casassa, J. Baima, S. Salustro *et al.*, *Wiley Interdiscip. Rev. Comput. Mol. Sci.* **8**, e1360 (2018).
- ¹²⁷O. Sugino and A. Oshiyama, *Phys. Rev. Lett.* **68**, 1858 (1992).
- ¹²⁸J. Yamauchi, M. Tsukada, S. Watanabe, and O. Sugino, *Phys. Rev. B* **54**, 5586 (1996).
- ¹²⁹S. Plimpton, *J. Comput. Phys.* **117**, 1 (1995).
- ¹³⁰J. Wellendorff, K. T. Lundgaard, A. Møgelhøj, V. Petzold, D. D. Landis, J. K. Nørskov, T. Bligaard, and K. W. Jacobsen, *Phys. Rev. B* **85**, 235149 (2012).
- ¹³¹BEEF calculations are not self-consistent and, thus, the forces on the atoms are not available. As such, energy derivatives must be used to evaluate the force constants.
- ¹³²S. Mukhopadhyay, D. S. Parker, B. C. Sales, A. A. Puretzky, M. A. McGuire, and L. Lindsay, *Science* **360**, 1455 (2018).
- ¹³³P. B. Allen and J. L. Feldman, *Phys. Rev. B* **48**, 12581 (1993).
- ¹³⁴J. L. Feldman, M. D. Kluge, P. B. Allen, and F. Wooten, *Phys. Rev. B* **48**, 12589 (1993).
- ¹³⁵W. Lv and A. Henry, *New J. Phys.* **18**, 013028 (2016).
- ¹³⁶L. Lindsay and D. A. Broido, *Phys. Rev. B* **81**, 205441 (2010).
- ¹³⁷A. Rohskopf, H. R. Seyf, K. Gordiz, T. Tadano, and A. Henry, *NPJ Comput. Mater.* **3**, 27 (2017).
- ¹³⁸X. Wu, Z. Liu, and T. Luo, *J. Appl. Phys.* **123**, 085109 (2018).